RECONFIGURABLE ALL-OPTICAL DE-MULTIPLEXING VIA SPATIAL-SELECTIVE FREQUENCY-UP-CONVERSION IN $\chi^{(2)}$ MULTIMODE WAVEGUIDE.

by

YOUNG BONG KWON

Presented to the Faculty of the Graduate School of

The University of Texas at Arlington in Partial Fulfillment

of the Requirements

for the Degree of

DOCTOR OF PHILOSOPHY

THE UNIVERSITY OF TEXAS AT ARLINGTON

May 2017

For my dear parents and Anna

Acknowledgements

First of all, I would like to express sincere appreciation to my academic advisor, Prof. Michael Vasilyev, for many reasons. Remembering last six years working with him, I am more realizing that the opportunities to learn under his guidance were truly a blessing for me. He allowed me to work for DARPA Quines program and I should confess that it is very valuable research opportunity. Also, his advice always worked for me to solve many challenging problems. His financial support enabled me to focus on the research. His patience toward me helped me to be more independent thinker. I ascribe my research fruits to him.

Next, I would like to express my gratidude to my wife and parents. My parents always supported me even at the times of my wandering. Without them, I might not be able to get through the many tough seasons. Their enduing love toward me was a powerful enough for me to stand-up again and again. I want to say thank to my sister. She has supported me with foods staying near Arlington. Also, her advice for life and school was always very valuable. My wife, Anna, is always the first person whom I can share my thought. She is also my good friend. We share the dream. We encourage each other. Now, we celebrate our graduation and believe we will get througth another life's adventures.

I would like to thank committee members, Professors Magnusson, Zhou, Chiao, and Sun. It is honor for me having such renowned scholars as my committee members. I appreciate their advices during my comprehensive exam and dissertation defense.

I also want to express appreciation to group members, Sarath, Lu, Mohan, Afshin, Kamanashis, Subrata, and Rouf. Through the diversity in their nationalities I was able to learn more about their cultures. Also, I will remember the conversations with them as happy memory.

April 21, 2017

Abstract

RECONFIGURABLE ALL-OPTICAL DE-MULTIPLXING
VIA SPATIAL-SELECTIVE FREQUENCY-UP-CONVERSION
IN $\chi^{(2)}$ MULTIMODE WAVEGUIDE.

Young Bong Kwon, PhD

The University of Texas at Arlington, 2017

Supervising Professor: Michael Vasilyev

We investigate spatial-mode-selective frequency up-converters in $\chi^{(2)}$ multimode waveguides for classical and quantum communication. For the classical application, our method works as spatial-mode de-multiplexer for mode-division-multiplexing (MDM) communication system. For the quantum application, mode-selective quantum frequency conversion (QFC) enables multidimensional quantum encoding (qudits rather than qubits) which could eventually contribute to higher capacity of quantum communication links (higher QKD rates).

First, we numerically investigate mode-selective up-conversion in a slab waveguide (2D free space) and periodically-polled KTP (PPKTP) waveguide. A 2D slab waveguide model is proposed based on non-collinear sum frequency generation (SFG). This model enables the calculation of conversion efficiencies of various spatial modes of the 2D slab waveguide by performing singular value decomposition (SVD) of Green's function. Next, the PPKTP waveguide is investigated to achieve mode-selective up-conversion. By proper tailoring of waveguide dimensions and quasi-phase-matching (QPM) period, we found two interesting scenarios. First scenario has application in image up-conversion, where a single pump mode simultaneously up-convert many signal modes. At the second scenario, a pump mode up-converts only a specific signal mode without

disturbing the rest of the modes, while simultaneously another pump mode up-converts another signal mode. The second scenario can be used for spatial-mode de-multiplexing, where any superposition of two signal modes can be selectively up-converted by the corresponding superposition of pump modes, while leaving the orthogonal signal superposition unperturbed.

Then, we implement the second scenario in periodically-poled lithium niobate (PPLN) waveguides, custom-made for us by Dr. Carsten Langrock in Prof. Martin Fejer's group at Stanford. Using these PPLN waveguides, we demonstrate four proof-of-concept experiments with different types of signals. The different signal types used for our experiments are continuous-wave (CW) classical (medium-power) and single-photon-level signals, 10-GHz data-modulated signal, and two-mode signal transmitted through a few-mode-fiber (FMF). To prove whether our method is suitable for the quantum application, we first demonstrate mode-selective up-conversion with CW classical signal and extend it to single-photon-level signal. For classical signals, we have observed conversion efficiency > 70% and crosstalk < –16 dB. For single-photon-level signals, we have observed conversion efficiency > 74%, crosstalk < –12 dB, and background noise at least 100 times lower than the signal. To prove that our method is suitable for the classical application in MDM communication system, we demonstrate mode-selective up-conversion with 10-GHz data-modulated two-mode signal, yielding < 2.5 dB crosstalk penalty at the 10^{-9} bit error rate level, as well as with a two-mode signal transmitted through an FMF, yielding > 46% conversion efficiency and < –14 dB crosstalk.

Our mode selection is performed by choosing the pump spatial profile and can be reconfigured at ~50 Hz rate. With several QPM gratings, the mode-selective up-conversion can be extended to a larger mode space and used for dynamically reconfigurable mode de-multiplexing.

Table of Contents

List of Illustrations

List of Tables

Chapter 1

INTRODUCTION

The mode-selective frequency-up-conversion is the theme for the dissertation. The main motivation is in contributions to the mode-division-multiplexing (MDM) communication system (classical application) and the higher dimensional quantum encoding enabling high quantum-key-distribution (QKD) rates (quantum application). Currently, needs for higher information capacity in fiber links rely on the wavelength division multiplexing (WDM) systems with advanced modulation formats such as quadrature amplitude modulation (QAM) and differential phase shift keying (DPSK). However, such WDM approaches have limited capabilities to catch the rapid growth of the demands on more information capacity. The MDM communication system, exploiting spatial domains rather than frequency domains, is considered as promising solution. To implement MDM system, a key functional block is the spatial-mode de-multiplexer. Such de-mulitplexers are usually implemented using "photonic lanterns," which separate the fiber output into mode groups (modes that have similar propagation constants, i.e. are degenerate). However, within each mode group there is a lot of inter-mode coupling, and electronic multiple-input-multiple-output (MIMO) processing is required to de-multiplex these degenerate modes, which is expensive. An alternative approach is a dynamically reconfigurable spatial-mode de-multiplexer (our method) based on mode-selective frequency conversion in a nonlinear waveguide. This is a motivation for our dissertation with respect to classical applications.

The mode-selective up-conversion is based on sum-frequency-generation (SFG). The SFG is also called quantum frequency conversion (QFC), which was first proposed by Kumar [1, 2], because QFC transfers the quantum statistical properties of the input signal modes to the up-converted modes. The QFC enables the use of high-efficiency, low-dark-count, inexpensive Si-based avalanche photodiodes (APD) rather than lower-efficiency, high-dark-count, and expensive InGaAs-based IR single-photon detectors. In addition, the QFC provides an interface between

telecom window and quantum memory, because the quantum memory is more easily implemented in the visible wavelength region. Inheriting these advantages of the QFC, the mode-selective frequency-up-conversion (or mode-selective QFC) may enable higher quantum key distribution (QKD) rates by using MDM fiber links or by high-dimensional quantum encoding using spatial degrees of freedom. This is a motivation of our dissertation with respect to quantum applications.

In prior work, temporal-mode-selective up-conversion was studied by several groups [3–5]. In spatial domain, spatial mode coupling in the parametric down-conversion process was investigated among vertical modes of a PPKTP waveguide [6, 7]. However, the vertical spatial modes of such a PPKTP waveguide are asymmetric and not suitable for fiber-coupling. In this dissertation, we use two-mode PPLN waveguide, whose modes are symmetric with >98% matching to free-space Hermite-Gaussian modes and are suitable for fiber coupling.

To implement the mode-selective up-conversion, we used a second-order nonlinear waveguide rather than free-space propagation in a bulk crystal. The nonlinear optical interaction in the waveguide is preferred over free-space interaction due to several reasons. First of all, the number of propagating modes can be controlled by adjusting the dimensions of the waveguide. Second, the modes confined to the smaller dimension of the waveguide result in higher nonlinear conversion efficiency. Third, we can use quasi-phase matching (QPM) technique to enable the collinear propagating of the signal, pump, and up-converted modes and easy phase-matching. After optimizing QPM conditions and waveguide dimensions, we achieve mode-selective frequency-up-conversion in a PPLN waveguide that supports two spatial modes, TM_{00} and TM_{01}, in the telecom wavelength region. In a scenario we found, a pump mode, TM_{00}, only up-converts signal mode, TM_{01}, without interrupting the other signal mode, TM_{00}. In the same PPLN waveguide, another pump mode, TM_{01}, only up-converts signal mode, TM_{00}, without interrupting the other signal mode, TM_{01}. Hence, by choosing a proper superposition of pump modes TM_{00} and

TM_{01} we can selectively up-convert any superposition of signal modes TM_{01} and TM_{00} without disturbing the orthogonal superposition of the signal modes.

In this dissertation, the spatial-mode-selective frequency-up-conversion is studied for the purpose of both classical and quantum applications, and is achieved by tailoring the mode dispersion properties via waveguide dimensions and phase-matching conditions via proper QPM period. In chapter 2, we do a numerical study for mode-selective up-conversion in a 1D slab waveguide. To do this, we develop a 2D free-space model based on SFG and study selective conversion by various HG modes combinations of the pump. In chapter 3, we numerically study 2D PPKTP waveguide with step-index in horizontal dimension and demonstrate two interesting scenarios, one of which could be used for image up-conversion, and the other – for mode-selective frequency-up-conversion (mode de-multiplexing). In chapter 4, we implement the latter scenario in a PPLN waveguide fabricated by our collaborators from Stanford University and demonstrate several prove-of-concept experiments based on different types of signal. The CW and single-photon-level signal experiments are demonstrated with the quantum communication application in mind, and experiments with 10-Gb/s data-modulated signal and with signal modes transmitted through a few-mode fiber (FMF) are demonstrated for classical communication application. In chapter 5, we make the conclusion of this research and propose future work for further investigation on this interesting research topic.

Young Bong Kwon's Publications

Journal papers

1. "Reconfigurable platform for processing of classic and quantum spatially-multimode signals," Y. B. Kwon, M. Giribabu, L. Li, S. C. Samudrala, C. Langrock, M. Fejer, M. Vasilyev, in preparation for submission to Optica.

2. "All-optical regenerator of multi-channel signals," L. Li, P. G. Patki, Y. B. Kwon, V. Stelmakh, B. Campbell, M. Annamalai, T. I. Lakoba, and M. Vasilyev, submitted to Nature Comm. (currently undergoing 2nd round of reviews).

Conferences

1. "Single-photon-level spatial-mode-selective frequency up-conversion in a multimode $\chi(2)$ waveguide," Y. B. Kwon, M. Giribabu, C. Langrock, M. Fejer, M. Vasilyev, to be presented at the CLEO 2017 conference, San Jose, CA, May 14–19, 2017, paper FF2E.1.

2. "Experimental demonstration of spatial-mode-selective frequency up-conversion in a multimode $\chi(2)$ waveguide," Y. B. Kwon, M. Giribabu, L. Li, S. C. Samudrala, C. Langrock, M. Fejer, and M. Vasilyev, CLEO 2016 conference, San Jose, CA, June 5–10, 2016, paper STh3P.4.

3. "2R Regeneration of 12 WDM Channels with 100-GHz Spacing in a Group-Delay-Managed Nonlinear Medium," L. Li, Y.-B. Kwon, B. Campbell, T. I. Lakoba, and M. Vasilyev, Optical Fiber Communication conference, Annaheim, CA, March 20–24, 2016, paper W4D.4.

4. "Demonstration of spatially selective frequency up-conversion in multimode PPLN," Y. B. Kwon and M. Vasilyev, UT Arlington Photonics Symposium, University of Texas at Arlington, Arlington, TX, September 14, 2015.

5. "Spatial-mode-selective quantum frequency conversion in nonlinear waveguides," M. Vasilyev and Y. B. Kwon, the Quantum Optics and Quantum Information Transfer and Processing conference (part of SPIE Optics + Optoelectronics), April 13–16, 2015, Prague, Czech Republic, paper 9505-25; Proc. SPIE 9505, 95050O (2015).

6. "Spatial-Mode-Selective Quantum Frequency Conversion in a $\chi(2)$ Slab Waveguide," M. Vasilyev, Y. B. Kwon, and Y.-P. Huang, the Quantum Information and Measurement (QIM) conference (part of OSA Research in Optical Sciences Congress), Berlin, Germany, March 18–20, 2014, paper JW2A.52.

7. "Mode-selective frequency up-conversion in a $\chi(2)$ waveguide," Y. B. Kwon and M. Vasilyev, the "Nonlinear Frequency Generation and Conversion: Materials, Devices, and Applications XIII" conference (part of SPIE LASE / Photonics West), February 1–6, 2014, San Francisco, CA, paper 8964-21; Proc. SPIE 8964, 8964-21.

8. "Highly mode-selective quantum frequency conversion in a slab waveguide," M. Vasilyev, Y. B. Kwon, and Y.-P. Huang, the "Advances in Photonics of Quantum Computing, Memory, and Communication VII" conference (part of SPIE OPTO / Photonics West), February 1–6, 2014, San Francisco, CA, paper 8997-22; Proc. SPIE 8997, 8997-22.

Chapter 2

THEORY OF SPATIAL-SELECTIVE FREQUENCY CONVERSION IN 2D SLAB WAVEGUIDE

2.1 Introduction

Following the current trends of classical long-distance communications, the future quantum communication links will aim to maximize their capacities/rates by utilizing multiple wavelengths, polarizations, and spatial modes of the fiber [8]. Hence, there is a need for spatial-mode-selective frequency up-converters of quantum states from infrared to visible region [1, 2, 9], which will be useful not only for interfacing the optical fiber links with quantum memories and for increasing the photon detection efficiency (both are well-known applications [10-12]), but also for demultiplexing of spatial modes that are otherwise difficult to discriminate in both spatial and spatial-frequency domains (see Fig. 2.1). The key to the quantum use of these devices is their ability to up-convert the desired mode with 100% efficiency without affecting any other spatially overlapping modes.

In the following sections, we discuss two such spatial-mode-selective quantum frequency converters. The first one is based on sum-frequency generation (SFG) in 2D free space (slab waveguide with one-dimensional confinement) and represents a straightforward extension of temporal-mode-selective SFG [3-5]. The eigenmodes of this 2D process can be found by performing singular value decomposition (SVD) of its Green's function [13, 14], and the resulting SVD spectrum (conversion efficiencies for different modes) can be controlled by properly adjusting the pump spatial profile. The second spatial-mode-selective frequency up-converter is based on a multimode waveguide with two-dimensional confinement. Here, the waveguide geometry defines the dispersion and, consequently, the phase-matching conditions for various combinations of signal, pump, and sum-frequency modes [15]. With proper quasi-phase-matching, one can approach 100% up-conversion of any mode superposition from a sub-space of several

lowest waveguide modes, without affecting any orthogonal mode superpositions, by properly choosing the pump mode profile.

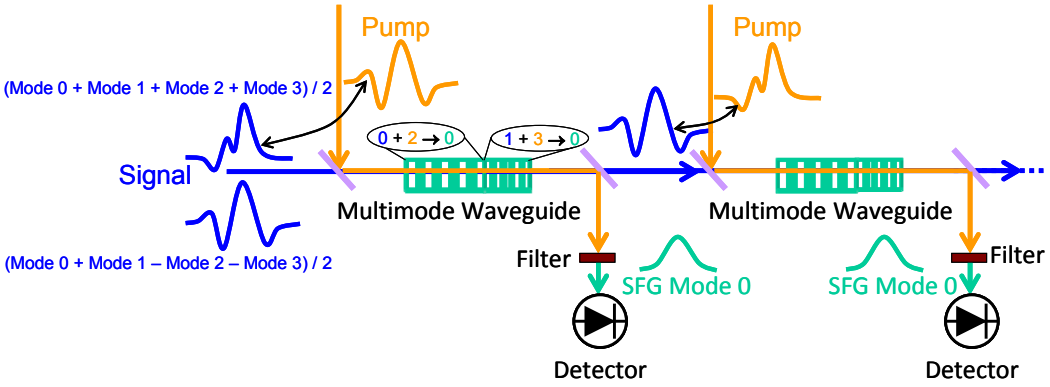

Figure 2-1. Proposed scheme of multi-dimensional selective frequency up-conversion. Using SFG to discriminate spatial modes of the signal by selectively up-converting the desired mode (or superposition of the modes) while leaving all the other modes undisturbed. Selection is performed by choice of the pump spatial profile. The procedure can be repeated for other modes.

2.2 MODE-SELECTIVE SUM-FREQUENCY GENERATION IN A SLAB WAVEGUIDE

Here we extend the approach of Ref. [5] from temporally-multimode to spatially-multimode signals. From a mathematics point of view, the propagation of pump and signal temporal pulses of different group velocities is equivalent to the non-collinear propagation of pump and signal beams of finite widths (lateral walk-off replaces temporal walk-off). The latter situation can be realized in a nonlinear $\chi^{(2)}$ slab waveguide, which confines light in one dimension (y) and permits free-space propagation in the other two dimensions (x,z) [see Fig. 2.2 (left)]. We build a model based on Green's function formalism for the SFG equations and perform singular-value decomposition (SVD) of the Green's function to find the eigenmodes for the signal and the sum-frequency waves. By adjusting the spatial profile of the pump, we manipulate the SVD spectrum to maximize the up-conversion of the first signal mode while minimizing the up-conversion of the rest of the modes. We show that, even though in the spatial case the pump and signal beams walk off in opposite directions from the SFG beam, which is a much worse situation than the situations

considered by [3, 5] in the temporal case, it is still possible to achieve a good mode discrimination by using a pump beam with appropriately-shaped spatial profile. This capability, when combined with the temporal-mode-selective up-conversion, can potentially lead to new quantum operations in a high-dimensional Hilbert space.

Let us consider non-collinear sum-frequency generation (SFG) in a 2D slab waveguide. Under geometrical optics approximation (no diffraction), the relevant regions of space for the three coupled waves are shown in Figure 2-2, with the following key features:

- For the process defined by $\omega_s + \omega_p = \omega_{SFG}$, where $\omega_s \approx \omega_p$, the geometrical optics approximation requires preservation of transverse momentum. Thus, for pump wave (index "*p*") propagating at an angle $-\alpha = -\tan^{-1}\beta$ with respect to *z*-axis (with *z*-direction being along the long side of the nonlinear crystal of length *L*), the signal wave (index "s") should propagate at an angle $+\alpha = +\tan^{-1}\beta$ with respect to *z*-axis, in order for the sum-frequency wave (index "SFG") to travel in *z*-direction.
- At the crystal input ($z = 0$), the pump has non-zero values only for $x \in [0, W]$. This leads to non-zero pump values within the diagonally shaded region of space in Figure 2-2, which provides coupling between the signal and SFG regions shown in Figure 2-2 by the green parallelogram and dotted rectangle, respectively.
- Considering all input ($z = 0$) values from these regions (i.e., $x \in [-2\beta L, W]$ for the signal wave and $x \in [-\beta L, W]$ for the SFG wave) is necessary for proper setting of initial conditions and obtaining the Green's function.
- The Green's function couples these input values to the output ($z = L$) values in the spatial regions $x \in [-\beta L, W+\beta L]$ for the signal wave and $x \in [-\beta L, W]$ (same region as at the input) for the SFG wave.

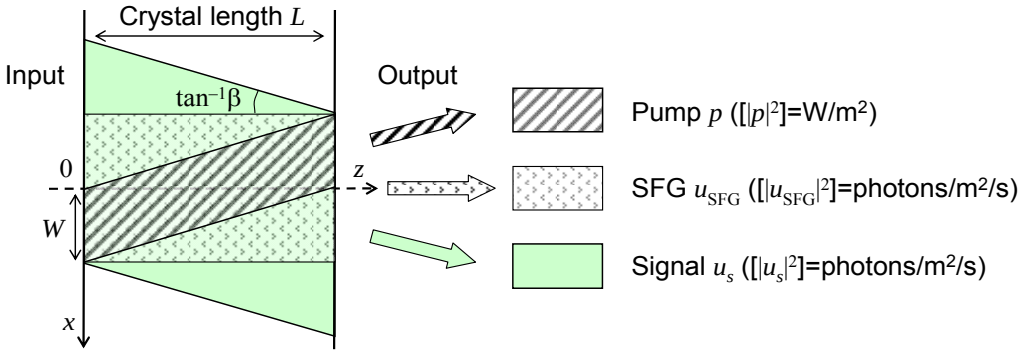

Figure 2-2 SFG problem definition in (x,z) plane.

In following discussion, we will consider the case where its full width displaces the pump beam after travelling through the crystal, i.e., $\beta L = W$, and compare it to the case of the z-propagating pump (i.e., $\beta = 0$).

Assuming the z-components of the three waves to be phase-matched or quasi-phase-matched, we can write the coupled three-wave equations with the undepleted pump as follows:

$$\begin{aligned} \frac{\partial w_p(x,z)}{\partial z} - \beta \frac{\partial w_p(x,z)}{\partial x} &= 0, \\ \frac{\partial u_s(x,z)}{\partial z} + \beta \frac{\partial u_s(x,z)}{\partial x} &= i\gamma w_p^*(x,z) u_{\mathrm{SFG}}(x,z), \\ \frac{\partial u_{\mathrm{SFG}}(x,z)}{\partial z} &= i\gamma w_p(x,z) u_s(x,z). \end{aligned} \tag{1.1}$$

where $\gamma = \sqrt{\frac{2d_{\mathrm{eff}}^2 \omega_s \omega_{\mathrm{SFG}} (1+\beta^2)}{n_s n_p n_{\mathrm{SFG}} \varepsilon_0 c^3}}$, and normalization is such that $|w_p|^2$ is the pump intensity and $|u_{s(\mathrm{SFG})}|^2$ is the photon flux (photons/m^2/s) of the signal (SFG) wave. The equation (1.1) can be re-written in a moving frame ($x \pm \beta z$) traveling in the negative (upper sign) or positive (lower sign) x-direction, along with the pump or signal envelope, respectively. It eliminates the partial derivative $\partial/\partial x$ from Eq. (1.1) at the expense of having to define boundary conditions on a tilted input line

$I(x,z)$. However, for $\beta << 1$, this line is approximately the same as line $z = 0$, and the system (1.1) is simplified into:

$$\begin{aligned} w_p(x,z) &= w_p(x+\beta z,0) = p(x+\beta z), \\ \frac{\partial}{\partial z}\begin{pmatrix} u_s(x-\beta z,z) \\ u_{\mathrm{SFG}}(x,z) \end{pmatrix} &= \begin{bmatrix} 0 & i\gamma p^*(x+\beta z) \\ i\gamma p(x+\beta z) & 0 \end{bmatrix}\begin{pmatrix} u_s(x-\beta z,z) \\ u_{\mathrm{SFG}}(x,z) \end{pmatrix}, \end{aligned} \tag{1.2}$$

with $p(x) = w_p(x,0) = |\, p(x) \,| \exp[i\theta(x)]$, and the initial conditions still defined at $z = 0$. Since the coupling matrix

$$\mathbf{M}(x) = \begin{bmatrix} 0 & i\gamma p^*(x+\beta z) \\ i\gamma p(x+\beta z) & 0 \end{bmatrix} \tag{1.3}$$

is anti-Hermitian (as a consequence, its eigenvalues are pairs of opposite imaginary numbers), the resulting Green's function is unitary (and its eigenvalues are pairs of complex conjugate numbers located on a unit circle).

Eliminating the x-derivative from Eq. (1.1) makes it very easy to compute the Green's function by direct integration of Eq. (1.2), using either analytical solution at each step with a mid-step pump value, or Runge-Kutta 4th-order (RK4): for example, in Matlab, one just supplies an identity matrix, instead of a vector, as an input; the output matrix is the Green's function. On the other hand, the original Eq. (1.1) and its diffraction-included version needs more complicated algorithms, such as split-step Fourier, which are not friendly to Green's function (input delta function immediately causes aliasing in frequency-domain) and require extensive workarounds.

The solution of Eq. (1.2) takes the following form:

$$\begin{pmatrix} u_s(x-\beta L,L) \\ u_{\mathrm{SFG}}(x,L) \end{pmatrix} = \int \begin{bmatrix} G_{11}(x-\beta L,x',L) & G_{12}(x-\beta L,x',L) \\ G_{21}(x,x',L) & G_{22}(x,x',L) \end{bmatrix}\begin{pmatrix} u_s(x',0) \\ u_{\mathrm{SFG}}(x',0) \end{pmatrix} \mathrm{d}x', \tag{1.4}$$

using the unitary Green's function matrix

$$\mathbf{G}=\begin{bmatrix} G_{11}(x-\beta L,x',L) & G_{12}(x-\beta L,x',L) \\ G_{21}(x,x',L) & G_{22}(x,x',L) \end{bmatrix}=\left(\mathbf{G}^{+}\right)^{-1}, \tag{1.5}$$

where superscript "+" stands for complete Hermitian conjugation, including switching the first and second arguments of the function.

Green's function of Eq. (1.5) can be represented by its singular value decomposition (SVD)

$$\mathbf{G}=\begin{bmatrix} \mathbf{U}_1(x-\beta L)\mathbf{t}\mathbf{V}_1^{+}(x') & i\mathbf{U}_1(x-\beta L)\mathbf{r}\mathbf{V}_2^{+}(x') \\ i\mathbf{U}_2(x)\mathbf{r}^{\mathbf{T}}\mathbf{V}_1^{+}(x') & \mathbf{U}_2(x)\mathbf{t}'\mathbf{V}_2^{+}(x') \end{bmatrix}, \tag{1.6}$$

where $\mathbf{U}_i(x)$ and $\mathbf{V}_i(x)$ are horizontal vectors (i = 1,2) with columns number j occupied by left- (output mode number j) and right- (input mode number j) singular functions $u_{ij}(x)$ and $v_{ij}(x)$, respectively, and $\mathbf{t}$, $\mathbf{t}'$ ($\mathbf{r}$) are square (rectangular) diagonal matrices with non-negative real numbers on the diagonal. Functions $u_{ij}(x)$ are orthonormal: $\int u_{ij}^{*}(x)u_{ik}(x)\,\mathrm{d}x=\delta_{jk}$; same holds for $v_{ij}(x)$. The only difference between $\mathbf{t}$ and $\mathbf{t}'$ is their dimensions: the larger one of them contains the same diagonal elements as the smaller one, with the rest of the diagonal filled up by unities. This decomposition represents 2×2 coupling of jth modes of input signal and SFG to the corresponding jth modes of the output:

$$\begin{pmatrix} b_{sj} \\ b_{\mathrm{SFG}j} \end{pmatrix}=\begin{bmatrix} t_j & ir_j \\ ir_j & t_j \end{bmatrix}\begin{pmatrix} a_{sj} \\ a_{\mathrm{SFG}j} \end{pmatrix}, \tag{1.7}$$

where t_j and r_j are jth singular values [i.e., jjth elements of matrices $\mathbf{t}$ and $\mathbf{r}$ in equation (1.6) equation reference goes hereEq. (1.6)] satisfying, $t_j^2+r_j^2=1$,

$$\begin{aligned} a_{sj}&=\int v_{1j}^{*}(x)u_s(x,0)\,\mathrm{d}x, \quad a_{\mathrm{SFG}j}=\int v_{2j}^{*}(x)u_{\mathrm{SFG}}(x,0)\,\mathrm{d}x, \\ b_{sj}&=\int u_{1j}^{*}(x)u_s(x,L)\,\mathrm{d}x, \quad b_{\mathrm{SFG}j}=\int u_{2j}^{*}(x)u_{\mathrm{SFG}}(x,L)\,\mathrm{d}x, \end{aligned} \tag{1.8}$$

are the input and output mode amplitudes.

The separate SVDs of four elements of Green's function $\mathbf{G}$, given by Eq. (1.6), is related to the SVD of the entire Green's function. Indeed, it is easy to see that for the input given by

$$\begin{pmatrix} u_s(x,0) \\ u_{\mathrm{SFG}}(x,0) \end{pmatrix} = \begin{pmatrix} v_{1j}(x) \\ \pm v_{2j}(x) \end{pmatrix} \tag{1.9}$$

Eqs. (1.4)–(1.6) lead to the output given by

$$\begin{pmatrix} u_s(x-\beta L, L) \\ u_{\mathrm{SFG}}(x,L) \end{pmatrix} = (t_j \pm i r_j) \begin{pmatrix} u_{1j}(x-\beta L) \\ \pm u_{2j}(x) \end{pmatrix} = e^{\pm i \tan^{-1}(r_j/t_j)} \begin{pmatrix} u_{1j}(x-\beta L) \\ \pm u_{2j}(x) \end{pmatrix}, \tag{1.10}$$

i.e., the entire Green's function can be written as

$$\begin{aligned} \mathbf{G} &= \begin{bmatrix} \dfrac{\mathbf{U}_1(x-\beta L)}{\sqrt{2}} & \dfrac{\mathbf{U}_1(x-\beta L)}{\sqrt{2}} \\ \dfrac{\mathbf{U}_2(x)}{\sqrt{2}} & -\dfrac{\mathbf{U}_2(x)}{\sqrt{2}} \end{bmatrix} \begin{bmatrix} \mathbf{t}+i\mathbf{r} & 0 \\ 0 & \mathbf{t}-i\mathbf{r} \end{bmatrix} \begin{bmatrix} \dfrac{\mathbf{V}_1(x')}{\sqrt{2}} & \dfrac{\mathbf{V}_1(x')}{\sqrt{2}} \\ \dfrac{\mathbf{V}_2(x')}{\sqrt{2}} & -\dfrac{\mathbf{V}_2(x')}{\sqrt{2}} \end{bmatrix}^{+} \\ &= \mathbf{U} \begin{bmatrix} \mathbf{t}+i\mathbf{r} & 0 \\ 0 & \mathbf{t}-i\mathbf{r} \end{bmatrix} \mathbf{V}^{+}, \end{aligned} \tag{1.11}$$

where the shorter of one vectors $\mathbf{U}_1$ and $\mathbf{U}_2$ (as well as the shorter one of $\mathbf{V}_1$ and $\mathbf{V}_2$) is padded with zeros, whereas the longer-vector components of the same index lose the factor $2^{1/2}$ in the denominator (for normalization). Dimensions of the diagonal matrices $\mathbf{t}$ and $\mathbf{r}$ are made to match those of the vectors by padding them with ones and zeros, respectively. The diagonal matrix in the middle is unitary, and the phases of its complex-conjugate eigenvalues can be absorbed into the phases of the corresponding columns of either $\mathbf{U}$ or $\mathbf{V}$, or (preferably) both. This creates new matrices $\mathbf{U}'$ or $\mathbf{V}'$, while the diagonal matrix in the middle becomes simply an identity matrix, yielding the following SVD of the Green's function:

$$\mathbf{G} = \mathbf{U}' \mathbf{V}'^{+}. \tag{1.12}$$

In some cases, the input and output mode sets are similar (e.g., in collinear propagation), then an eigenvalue decomposition of the Green's function can provide adequate information about the

input-output transformation. In a more general case, however, the output modes are different from the input modes, and SVD of either element of [see Eq. (1.6)] or entire [see Eq. (1.12)] Green's function is needed to find the 2×2 coupling between the pairs of input and output modes.

2.2.1 *Case 1: Pump propagating in z-direction* ($\beta = 0$)

In this case, the coupling coefficients in Eq. (1.2) are independent of z, and the anti-Hermitian coupling matrix

$$\mathbf{M}(x) = \begin{bmatrix} 0 & i\gamma p^{*}(x) \\ i\gamma p(x) & 0 \end{bmatrix} \tag{1.13}$$

leads to the solution

$$\begin{pmatrix} u_s(x,z) \\ u_{\mathrm{SFG}}(x,z) \end{pmatrix} = e^{\mathbf{M}(x)z} \begin{pmatrix} u_s(x,0) \\ u_{\mathrm{SFG}}(x,0) \end{pmatrix}, \tag{1.14}$$

with the Green's function

$$\mathbf{G} = e^{\mathbf{M}(x)z}\ \delta(x - x'). \tag{1.15}$$

Due to the unitarity of the transformation, all eigenvalues of the Green's function (1.15) are located on a unit circle in the complex plane, and for each eigenvalue, there is another complex conjugate eigenvalue. The eigenvalue decomposition of the Green's function (1.15) is given by

$$\begin{aligned} \mathbf{G} &= \mathbf{S} \begin{bmatrix} e^{i\gamma|p(x)|z} & 0 \\ 0 & e^{-i\gamma|p(x)|z} \end{bmatrix} \mathbf{S}^{+}\, \delta(x - x') \\ &= \begin{bmatrix} \cos[\gamma\,|\,p(x)\,|\,z] & ie^{-i\theta(x)} \sin[\gamma\,|\,p(x)\,|\,z] \\ ie^{i\theta(x)} \sin[\gamma\,|\,p(x)\,|\,z] & \cos[\gamma\,|\,p(x)\,|\,z] \end{bmatrix} \delta(x - x'), \end{aligned} \tag{1.16}$$

where

$$\mathbf{S} = \begin{bmatrix} \mathbf{u}_1 & \mathbf{u}_2 \end{bmatrix} = \begin{bmatrix} \dfrac{e^{-i\theta(x)/2}}{\sqrt{2}} & \dfrac{e^{-i\theta(x)/2}}{\sqrt{2}} \\ \dfrac{e^{i\theta(x)/2}}{\sqrt{2}} & -\dfrac{e^{i\theta(x)/2}}{\sqrt{2}} \end{bmatrix}, \tag{1.17}$$

and

$$\mathbf{u}_1 = \begin{pmatrix} \dfrac{e^{-i\theta(x)/2}}{\sqrt{2}} \\ \dfrac{e^{i\theta(x)/2}}{\sqrt{2}} \end{pmatrix}, \quad \mathbf{u}_2 = \begin{pmatrix} \dfrac{e^{-i\theta(x)/2}}{\sqrt{2}} \\ -\dfrac{e^{i\theta(x)/2}}{\sqrt{2}} \end{pmatrix} \tag{1.18}$$

are the eigenvectors corresponding to the eigenvalues $\lambda_1 = e^{i\gamma|p(x)|z}$ and $\lambda_2 = \lambda_1^* = e^{-i\gamma|p(x)|z}$, respectively. The solution (1.14) can be re-written as

$$\begin{pmatrix} u_s(x,z) \\ u_{\mathrm{SFG}}(x,z) \end{pmatrix} = A(x)e^{i\gamma|p(x)|z}\mathbf{u}_1 + B(x)e^{-i\gamma|p(x)|z}\mathbf{u}_2\,, \tag{1.19}$$

where

$$\begin{aligned} A(x) &= \frac{u_s(x,0)e^{i\theta(x)/2} + u_{\mathrm{SFG}}(x,0)e^{-i\theta(x)/2}}{\sqrt{2}}\,, \\ B(x) &= \frac{u_s(x,0)e^{i\theta(x)/2} - u_{\mathrm{SFG}}(x,0)e^{-i\theta(x)/2}}{\sqrt{2}} \end{aligned} \tag{1.20}$$

have been obtained from the initial conditions. Alternatively, Eq. (1.19) can be re-written in the form

$$\begin{aligned} \begin{pmatrix} u_s(x,z) \\ u_{\mathrm{SFG}}(x,z) \end{pmatrix} = &\left\{ u_s(x,0)e^{i\theta(x)/2}\frac{\mathbf{u}_1+\mathbf{u}_2}{\sqrt{2}} + u_{\mathrm{SFG}}(x,0)e^{-i\theta(x)/2}\frac{\mathbf{u}_1-\mathbf{u}_2}{\sqrt{2}} \right\}\cos\left[\gamma\,|\,p(x)\,|\,z\right] \\ &+ \left\{ iu_s(x,0)e^{i\theta(x)/2}\frac{\mathbf{u}_1-\mathbf{u}_2}{\sqrt{2}} + iu_{\mathrm{SFG}}(x,0)e^{-i\theta(x)/2}\frac{\mathbf{u}_1+\mathbf{u}_2}{\sqrt{2}} \right\}\sin\left[\gamma\,|\,p(x)\,|\,z\right], \end{aligned} \tag{1.21}$$

which highlights a pair of two-frequency modes (the expressions in the curly brackets) of which we have a cosine/sine transfer of energy/information. Noting that

$$\begin{aligned} e^{i\theta(x)/2}\frac{\mathbf{u}_1+\mathbf{u}_2}{\sqrt{2}} &= \begin{pmatrix} 1 \\ 0 \end{pmatrix}, \\ e^{-i\theta(x)/2}\frac{\mathbf{u}_1-\mathbf{u}_2}{\sqrt{2}} &= \begin{pmatrix} 0 \\ 1 \end{pmatrix}, \end{aligned} \tag{1.22}$$

one can re-write Eq. (1.21) as

$$\begin{pmatrix} u_s(x,z) \\ u_{\mathrm{SFG}}(x,z) \end{pmatrix} = \left\{ u_s(x,0)\cos\left[\gamma \mid p(x) \mid z\right] + iu_{\mathrm{SFG}}(x,0)e^{-i\theta(x)}\sin\left[\gamma \mid p(x) \mid z\right] \right\} e^{i\theta(x)/2}\frac{\mathbf{u}_1 + \mathbf{u}_2}{\sqrt{2}} + \left\{ u_{\mathrm{SFG}}(x,0)\cos\left[\gamma \mid p(x) \mid z\right] + iu_s(x,0)e^{i\theta(x)}\sin\left[\gamma \mid p(x) \mid z\right] \right\} e^{-i\theta(x)/2}\frac{\mathbf{u}_1 - \mathbf{u}_2}{\sqrt{2}} \tag{1.23}$$

and obtain another form for the solution:

$$\begin{pmatrix} u_s(x,z) \\ u_{\mathrm{SFG}}(x,z) \end{pmatrix} = \begin{bmatrix} \cos\left[\gamma \mid p(x) \mid z\right] & ie^{-i\theta(x)}\sin\left[\gamma \mid p(x) \mid z\right] \\ ie^{i\theta(x)}\sin\left[\gamma \mid p(x) \mid z\right] & \cos\left[\gamma \mid p(x) \mid z\right] \end{bmatrix} \begin{pmatrix} u_s(x,0) \\ u_{\mathrm{SFG}}(x,0) \end{pmatrix}. \tag{1.24}$$

A solution of Eq. (1.24) can also be obtained by combining Eqs. (1.14), (1.15), and (1.16).

If one performs a singular value decomposition (SVD) of G_{21} portion of the Green's function of Eq. (4), for z-propagating pump case one obtains the singular values given by $|\sin[\gamma|p(x)|z]|$ and left- and right-singular vectors given by $\delta(x–x')$.

2.2.2 *Case 2: Pump propagating at an angle* $\tan^{-1}\beta$, *where* $\beta = W / L$

This case has to be treated numerically in Matlab, using signal $\mathbf{u}_s$ and SFG $\mathbf{u}_{\mathrm{SFG}}$ as vertical vectors of dimensions $n_s = 3\,(n_p–1) + 1$ and $n_{\mathrm{SFG}} = 2\,(n_p–1) + 1$ (these correspond to points in x-dimension), respectively, with $n_p = 201$ (number of the pump points in x-dimension). At each of $n_z = (n_p – 1) / 2$ steps, we use the analytical solution with a mid-step pump value:

$$\begin{pmatrix} \mathbf{u}_s(z+h) \\ \mathbf{u}_{\mathrm{SFG}}(z+h) \end{pmatrix} = \cos\left[\sqrt{-\mathbf{M}^2(z+h/2)}\,h\right] * \begin{pmatrix} \mathbf{u}_s(z) \\ \mathbf{u}_{\mathrm{SFG}}(z) \end{pmatrix} + \left\{ \exp[i\arg(\mathbf{M}(z+h/2))].*\sin\left[\,|\mathbf{M}(z+h/2)|h\right] \right\} * \begin{pmatrix} \mathbf{u}_s(z) \\ \mathbf{u}_{\mathrm{SFG}}(z) \end{pmatrix}, \tag{1.25}$$

where $\mathbf{M}$ is $(n_s + n_{\mathrm{SFG}}) \times (n_s + n_{\mathrm{SFG}})$ coupling matrix given by Eq. (3), and $h = 2\,L\,/\,(n_p – 1)$ is the step size in z-dimension. In Eq. (25) we use Matlab notations of ".*" and "*" to denote element-by-element and matrix multiplication operations, respectively. In addition, $\mathbf{M}^2$ corresponds to matrix multiplication by itself, whereas all other functions (sine, cosine, exp, and square root) correspond to functions applied on element-by-element basis. Green's function of Eq.

(5) is obtained at the output by supplying an $(n_s + n_{SFG}) \times (n_s + n_{SFG})$ identity matrix instead of a vector at the input.

As the simplest case, we consider flat distribution of the pump intensity with $\gamma p(x)L = \pi$. In that case, the middle portion of the signal field interacts with the pump over distance $L / 2$, which, in the absence of reverse (SFG to signal) conversion process, would have resulted in 100% conversion efficiency (because $\sin[\gamma p(x)L/2] = 1$). With an eye on more complicated pump profiles, we introduce a factor

$$R = \frac{\gamma \max[|\, p(x)\,|]L}{\pi}, \tag{1.26}$$

which represents relative strength of pump field in various cases. For currently considered simplest case, R = 1. The results are shown in Figure 2-3: (left) – fundamental mode #0 (conversion efficiency 99.8%), (right) – mode #1 (conversion efficiency 56.2%). The conversion efficiency $|r_j|^2$ is plotted versus mode number j in Figure 2-4.

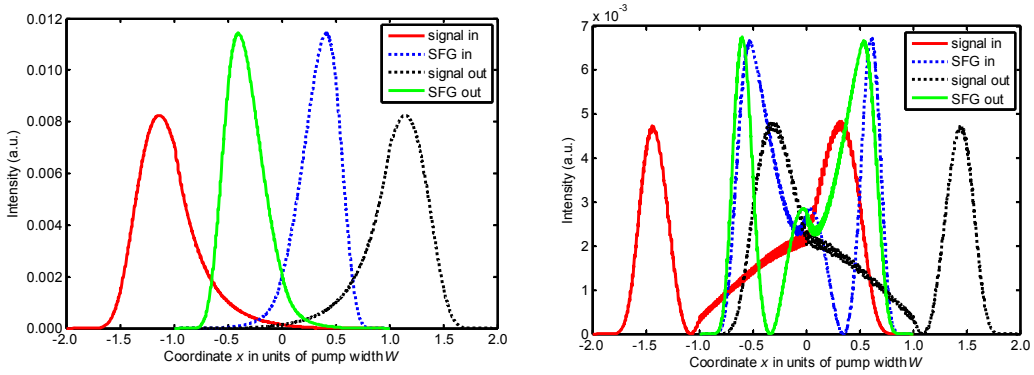

Figure 2-3 Input and output mode profiles for mode #0 (left) and mode #1 (right) for the case of flat pump profile with width W and $R = 1$.

If the power of the flat pump is decreased, the conversion efficiency of mode #0 goes down. If the power is increased, the conversion efficiencies for higher-order modes go up. If only a fraction of the total pump width W is occupied by a flat-top pump, while the power is kept constant (i.e., intensity is increased accordingly), there is virtually no change in the efficiency

difference between modes #0 and #1, but the efficiency for some of the higher modes gradually goes up.

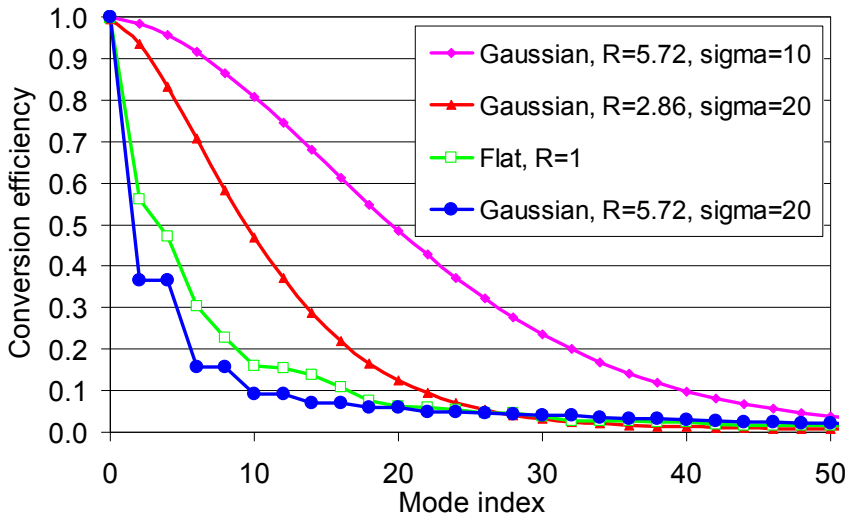

Figure 2-4 Conversion efficiency versus mode index for flat and Gaussian pump profiles.

Let us consider next the case of a pump with Gaussian field distribution with standard deviation $\sigma = W / 10 = 20$ points. We have found a nice sharp conversion efficiency spectrum for $R = 5.72$, where efficiencies for mode #0 and #1 (degenerate with #2) are 100% and 36.5%, respectively, as shown in Fig. Figure 2-4. The mode shapes are shown in Figure 2-5. Both increase ($R = 11.44$) and decrease ($R = 2.86$) of the power from the optimum value result in flattening of the conversion efficiency curves in Figure 2-4. We also compare these curves with the case of narrower ($\sigma = W / 20 = 10$ points) pump with $R = 5.72$ (i.e., peak intensity is the same as for wider pump with $R = 2.86$). The corresponding curve further flattens even compared to $R = 2.86$ case of the wider pump.

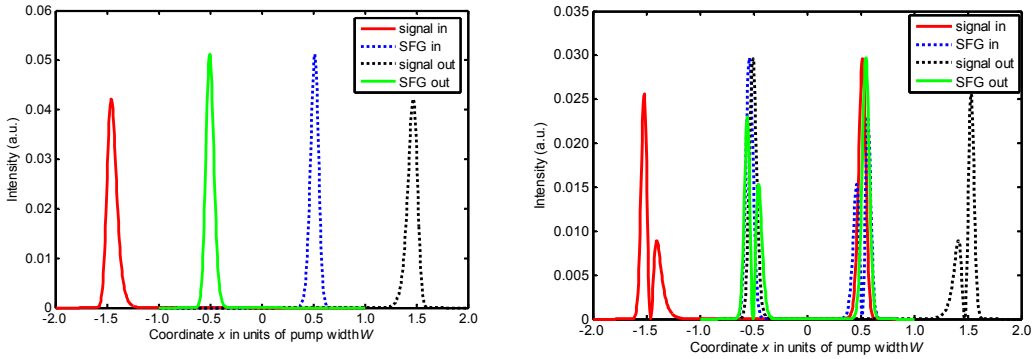

Figure 2-5 Input and output mode profiles for mode #0 (left) and mode #1 (right) for the case of Gaussian pump field profile with standard deviation $\sigma = W / 10 = 20$ points and $R = 1$.

2.3 Optimization by pump profile with multiple HG modes

We have optimized the pump profiles to further lower the up-conversion of the unwanted modes while keeping 100% conversion of the fundamental mode. Figure 2-6 shows the suppression of the unwanted-modes' up-conversion to 28%–30% by employing pump consisting of a superposition of 3–5 Hermite-Gaussian modes (left), as well as the corresponding pump profiles (right). By exploring HG spaces of up to 26 terms, we have concluded that this is a hard limit on what is achievable in the cross-beam SFG case. For larger discrimination between the first and second mode, a more advantageous arrangement of co-propagating signal and pump (and SFG wave propagating at an angle), emulating the time-domain case, is needed. Although the practical feasibility of such an arrangement is not clear (QPM in the transverse direction is required), we have developed the SFG mode solver for this case.

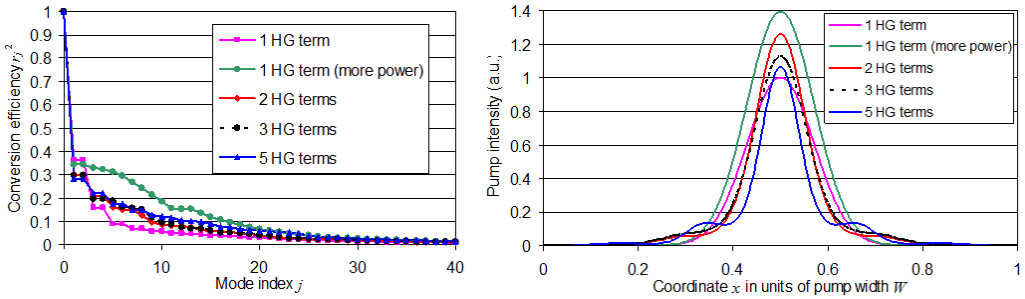

Figure 2-6 conversion efficiency and pump profile
(Left) Conversion efficiency spectra for pump profiles including various numbers of non-zero HG terms. (Right) Corresponding optimum pump profiles.

2.4 Optimization by solving inverse problem

Secondly, we have numerically solved a number of inverse problems on finding the arbitrary pump profile in form of HG-polynomial that ensure nealy-100% up-conversion for a given signal mode while minimizing up-conversion for another given mode. The extensive numerical optimization on weight of each HG-polynomial for pump profile allow discrimination between spatially-overlapping HG signal modes.

For Hermite-Gaussian signal modes HG0 and HG1, we have achieved 92.1% up-conversion of mode HG0 with 11.7 dB suppression of conversion of HG1, as well as 95.9% up-conversion of mode HG1 with 16.0 dB suppression of conversion of HG0.

For Hermite-Gaussian signal modes HG0 and HG2, we have achieved 98.8% up-conversion of mode HG0 with 14.4 dB suppression of conversion of HG2 (3.6%), as well as 96.7% up-conversion of mode HG2 with 12.3 dB suppression of conversion of HG0 (5.7%). Optimum pumps consisted of superpositions of 12 HG modes, as shown in Figure 2-7.

We have confirmed the robustness of discrimination between select spatially-overlapping Hermite-Gaussian signal modes. The pump profile enabling ~90% conversion of one mode with

>11 dB suppression of the other is not unique and can be tweaked to meet practical experimental constraints.

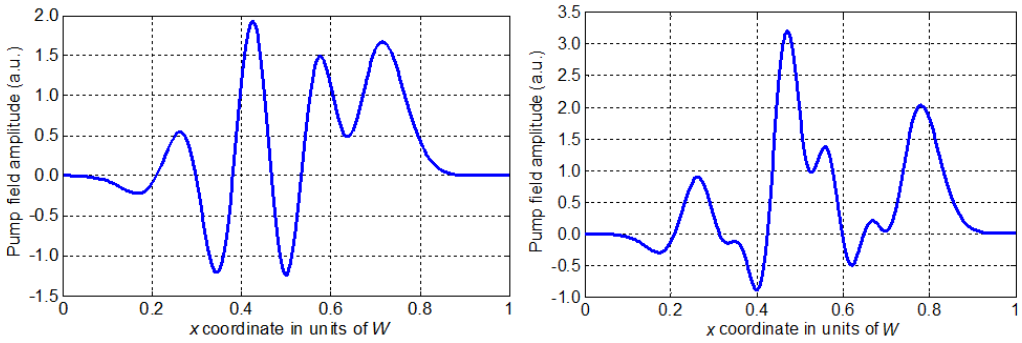

Figure 2-7 Optimized pump profiles
(Left): 12-HG-polynomial pump profile achieving 98.8% up-conversion of mode HG0 with 14.4 dB suppression of conversion of HG2. (Right): 12-HG-polynomial pump profile achieving 96.7% up-conversion of mode HG2 with 12.3 dB suppression of conversion of HG0.

2.5 Conclusions

We have developed a model for modal decomposition of sum-frequency generation process in a 2D free-space system (slab waveguide). Preliminary results indicate that, while 100% efficiency for fundamental mode #0 is achievable, the process is not quite single-mode (mode #1 conversion efficiency is above 36%). A subsequent numerical optimization of the pump profile has improved the suppression of the second mode from 36.5% to 28%–30% using a superposition of 3–5 lowest-order even Hermite-Gaussian modes. Finally, we solved inverse optimization problem such that HG0 signal achieved 98.8% conversion efficiency with 14.4 dB suppression of conversion of HG2 signal with optimized pump profile. Simultaneously, The HG2 signal achieved 96.7% up-conversion efficiency with 12.3 dB suppression of conversion of HG0 with another optimized pump profile.

Chapter 3

NUMERICAL MODELING OF MODE-SELECTIVE UP-CONVERSION IN $\chi^{(2)}$ MULTIMODE WAVEGUIDE

3.1 Introduction

Parametric amplification and frequency conversion of spatially-multimode light have been recently gaining attention in both classical and quantum signal-processing contexts, owing mostly to the emergence of the space-division multiplexing and mode-division multiplexing communication systems. Multimode parametric amplifiers [16-18], especially those capable of noiseless phase-sensitive amplification [19-21], could be an attractive solution for inline amplification in these systems, whereas "1550-nm-to-visible" frequency converters can be used to discriminate among various spatial modes and to improve the single-photon detection efficiency. Indeed, an efficient discrimination and demultiplexing of spatially-overlapping, but orthogonal, spatial modes, is an important active problem in current research. In addition, each resolved spatial mode needs to be efficiently detected. The efficient detection of faint (single-photon-level) infrared signals is important not only for communications, but also for military, biomedical, and quantum-optics applications. The dark counts of infrared avalanche photodetectors (APDs) based on InGaAs are much higher than those of silicon detectors operating in visible range. The noisy infrared detection can be avoided by converting signal photons from infrared to visible by means of sum frequency generation (SFG). Recent efforts on highly-efficient, low-noise, tunable single photon detection based on SFG in periodically-poled nonlinear crystals are discussed in [10-12]. Infrared-to-visible frequency conversion is especially attractive in quantum information applications, where avoidance of noise is critical. The unitary nature of the SFG process permits preservation of the signal quantum state in the conversion, which has lead to the proposal [1] and realization [2] of the quantum frequency conversion, and is currently being investigated for

spatially-multimode quantum states [9] (whereas the frequency conversion of a classical image was discussed by Midwinter back in 1968 [22]).

To achieve high conversion efficiencies at practical levels of pump power, it is beneficial to use multimode waveguides. The spatial mode couplings during second-harmonic generation were previously discussed in [23, 24]. Integrated mode converters and advanced quasi-phase-matching techniques for coupling odd and even modes were developed for waveguide-based SFG [25, 26]. Recently, the mode couplings in the spontaneous parametric down-conversion process were observed in vertically-multimode periodically-poled potassium titanyl phosphate (PPKTP) waveguides [6, 7].

In the following sections, we discusses a frequency converter realizable in a 20×6 μm^2 horizontally-multimode PPKTP waveguide. We show that under proper quasi-phase-matching, it can support one of the two spatial-mode-selective up-conversion scenarios. In the first scenario, a single pump mode can up-convert several different signal modes to different SFG modes, which is similar to an image up-conversion. In the second scenario, one pair of signal and pump modes is converted to an SFG mode and, at the same time, a different pair of signal and pump modes is up-converted to the same SFG mode. In that case, by adjusting the relative phases and magnitudes of the two pump modes, one can select for up-conversion any superposition of the two corresponding signal modes, without affecting the orthogonal superposition or any other modes. The latter scenario can be used for dynamically reconfigurable spatial-mode demultiplexing in both classical and quantum communications.

3.2 Background

3.2.1 Index Profile

Potassium titanyl phosphate (KTP) is one of crystals used widely for frequency conversion due to its high nonlinear-optical coefficient. Because KTP has high optical damage threshold, it is also suitable for high power applications. Bulk KTP can be grown by flux grown

technique or hydrothermal technique, and waveguide KTP can be fabricated on bulk KTP using ion-exchange with lithographic mask. Depending on the ions used for ion-exchange technique, both the waveguide diffusion depth and refractive index difference between the bulk KTP and waveguide can be changed. It is also known that the refractive index depth profile of Rb-ion-based KTP waveguide is close to complementary error function (Erfc). More detailed information about optical and mechanical properties and growth methods of KTP can be found in [27, 28].

To investigate mode properties of waveguide KTP, its effective refractive index needs to be known. Since the analytical solution of wave equation is not known for Erfc function depth profile, we have used the commercial numerical simulation package BeamProp from RSoft to find the effective refractive index. The waveguide is formed within a KTP substrate, and its transverse index profile is given by

$$\Delta n = 0.02 \times \mathrm{rect}\left(\frac{x}{W}\right) \times \mathrm{Erfc}\left(\frac{y}{D}\right), \tag{2.1}$$

i.e., is rectangular with width W = 20 μm in horizontal (x) direction and has Erfc function profile with depth D = 6 μm in vertical (y) direction. To find the effective index, x and y grid sizes were set to 0.06 μm, and z-direction step size was set to 0.5 μm in Beamprop. These parameters were carefully selected to balance the required accuracy and reasonable running time of the simulation.

3.2.2 Index dispersion

Quasi-phase-matching (QPM) both enables non-critical phase matching in KTP and permits taking advantage of the highest nonlinear coefficient, d_{33}, by using z-polarization for all three electric fields involved in the frequency up-conversion process. The wavelength-dependent refractive index can be calculated using Sellmeier equation [28].

$$n_z^2 = 2.25411 + \frac{1.06543}{1 - 0.05486\,\lambda^{-2}} - 0.02140\,\lambda^2. \tag{2.2}$$

Numerical simulation generates the effective index and mode profile of each propagating mode at signal, pump, and sum-frequency wavelengths. Due to a small size of the waveguide, it supports only a few propagating spatial modes. Figures 1 and 2 show the spatial mode profiles at the SFG and signal/pump wavelengths, respectively. Although the total number of SFG spatial modes at 0.775 μm is 14, we only show the first 12 modes.

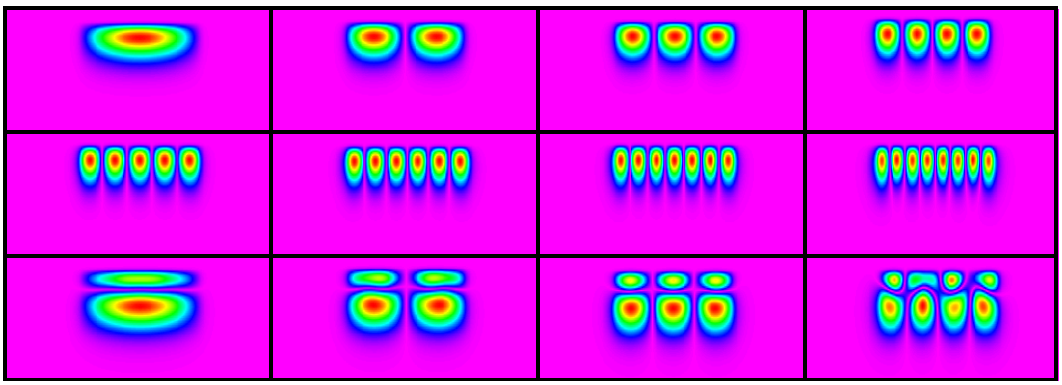

Figure 3-1 Spatial mode profiles of the SFG modes at 0.775 μm.
The top row corresponds to modes from 0 to 3. The second and third rows correspond to modes 4–7 modes 8–11, respectively.

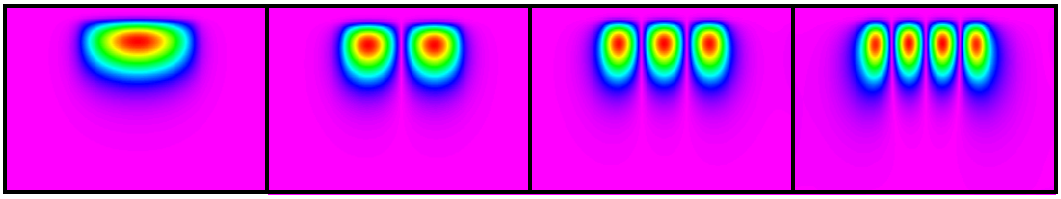

Figure 3-2 Spatial mode profiles of the signal modes at 1.54 μm
which are very similar to the pump modes at 1.56 μm. Modes from 0 to 3 are shown from left to right.

3.2.3 Phase mismatch tolerance and crystal length

The phase mismatch of QPM can be written as

$$\Delta k = \frac{2\pi}{\lambda_{\mathrm{SFG}}} n_{\mathrm{SFG}p}^{\mathrm{eff}} - \frac{2\pi}{\lambda_S} n_{Sm}^{\mathrm{eff}} - \frac{2\pi}{\lambda_P} n_{Pn}^{\mathrm{eff}} - \frac{2\pi}{\Lambda}, \tag{2.3}$$

where λ is the wavelength, n^{eff} is the effective index, Λ is the poling period of KTP waveguide, and indices *Sm*, *Pn*, and SFG*p* refer to the m^{th} signal mode, n^{th} pump mode, and p^{th} SFG mode, respectively. By dividing both sides of Eq. (2.3) by 2π, we can re-write it as

$$\Delta = \Delta'_{mnp} - \Delta_{\text{QPM}}\,, \tag{2.4}$$

where $\Delta_{\text{QPM}} = 1/\Lambda$, and

$$\Delta'_{mnp} = \frac{n_{\text{SFG}p}^{\text{eff}}}{\lambda_{\text{SFG}}} - \frac{n_{Sm}^{\text{eff}}}{\lambda_S} - \frac{n_{Pn}^{\text{eff}}}{\lambda_P} \tag{2.5}$$

is the mismatch between the m^{th} signal mode and n^{th} pump mode, on one hand, and the p^{th} SFG mode, on the other hand. We have chosen the wavelengths of the signal and pump to be $\lambda_S = 1.54$ μm and $\lambda_P = 1.56$ μm, respectively, which yields the SFG wavelength $\lambda_{\text{SFG}} = 0.775$ μm. We calculate the mismatch values Δ'_{mnp} for various combinations <*m*, *n*, *p*> (where order corresponds to <signal mode's index, pump mode's index, SFG mode's index>) Then, we inspect each combination to check whether there are any other combinations' mismatch values in its vicinity within a degree of tolerance related to the crystal length *L*. The output SFG intensity is given by [29]

$$I_{\text{SFG}}(\Delta k) = I_{\text{SFG}}(0)\ \text{sinc}^2\left(\frac{\Delta kL}{2}\right), \tag{2.6}$$

where $I_{\text{SFG}}(0)$ is the output SFG intensity for $\Delta k = 0$. The crystal length maximizing the SFG intensity is $L = \pi / |\Delta k| = 1 / (2|\Delta|)$.

For a finite-size crystal and chosen QPM period Λ, we would like the phase mismatch values $\Delta = \Delta'_{mnp} - \Delta_{\mathrm{QPM}}$ for all desired SFG combinations <*m*, *n*, *p*> to satisfy $|\Delta| \le 1 / (2L)$, i.e., to have all these processes phase-matched simultaneously. At the same time, we would like to keep the mismatches for all undesirable combinations at $|\Delta| >> 1 / (2L)$, so that the contribution of these processes is negligible.

3.2.4 Overlap integral

In addition to phase-matching, the up-conversion requires non-zero spatial overlap among the spatial modes of the three involved fields. More specifically, for <*m*, *n*, *p*> process the undepleted pump approximation yields the output SFG power given by

$$P_{\mathrm{SFG}p} = \eta L^2 \Phi_{mnp} P_{Sm} P_{Pn} \mathrm{sinc}^2\left(\frac{\Delta kL}{2}\right), \tag{2.7}$$

where $\eta = \dfrac{8\pi^2 d_{\mathrm{eff}}^2}{n_S^{\mathrm{eff}} n_P^{\mathrm{eff}} n_{\mathrm{SFG}}^{\mathrm{eff}} c\varepsilon_0 \lambda_{\mathrm{SFG}}^2}$ and

$$\Phi_{mnp} = \frac{\left|\int \Psi_{Sm}(\vec{\rho}) \Psi_{Pn}(\vec{\rho}) \Psi_{\mathrm{SFG}p}^*(\vec{\rho}) \mathrm{d}^2\vec{\rho}\right|^2}{\int \left|\Psi_{Sm}(\vec{\rho})\right|^2 \mathrm{d}^2\vec{\rho} \int \left|\Psi_{Pn}(\vec{\rho})\right|^2 \mathrm{d}^2\vec{\rho} \int \left|\Psi_{\mathrm{SFG}p}^*(\vec{\rho})\right|^2 \mathrm{d}^2\vec{\rho}} = \frac{1}{A_{\mathrm{eff}}} \tag{2.8}$$

is the overlap integral for the <*m*, *n*, *p*> combination, which has the physical meaning of the inverse effective area of this process.

The symmetry considerations produce zero overlap integral when the product of three modes is odd, i.e., when either only one of them is odd or all three of them are odd. Hence, these cases are excluded from the mode combinations studied here.

3.3 Results / Discussion

3.3.1 Case1

In the Case 1 scenario, pump spatial mode n is the same for two mode combinations $<m_1, n, p_1>$ and $<m_2, n, p_2>$, but both signal modes and sum frequency modes are different. This is similar to image up-conversion where multiple spatial modes are simultaneously up-converted. Such multimode frequency up-converter might have potential benefit for classical LIDARs as well as for quantum information systems exploiting spatial quantum correlations. Figure 3-3 shows the overlap integrals Φ_{mnp} (i.e., relative strengths of interactions) as a function of phase mismatch Δ'_{mnp} for various $<m, n, p>$ processes, where three possible Case 1 arrangements are shown with red arrows. It is important to make sure that no other mode combinations exist in the vicinity within tolerance, otherwise unwanted mode combination will also be simultaneously phase-matched. It is worth noting that the conjugate combinations $<m, n, p>$ and $<n, m, p>$ are almost degenerate in phase mismatch, i.e., these processes always occur together. This, however, is not a problem for the Case 1, because this case assumes only one strong pump mode n present at the input.

Table 1 summarizes detailed information for Case 1 mode combinations, such as mismatch value, effective area, and difference of mismatch value between the mode combinations. The effective area is the inverse of the corresponding overlap integral indicating the strength of interaction. The smaller the effective area is, the stronger the interaction is. The difference between the mismatches needs to be small, as discussed previously, to allow longer crystal length (Δ_{QPM} should be chosen somewhere in the middle between the mismatches of the desirable combinations). For mode combinations $<m, n, p>$ where numbers m, n, p cannot form a triangle (i.e., one of them is greater than the sum of the others), the effective area becomes very large, indicating reduced interaction strengths. This is qualitatively similar to the case of a parabolic-

index waveguide, where triangle rule is a strict selection rule, and non-triangle combinations have exactly zero overlap integral.

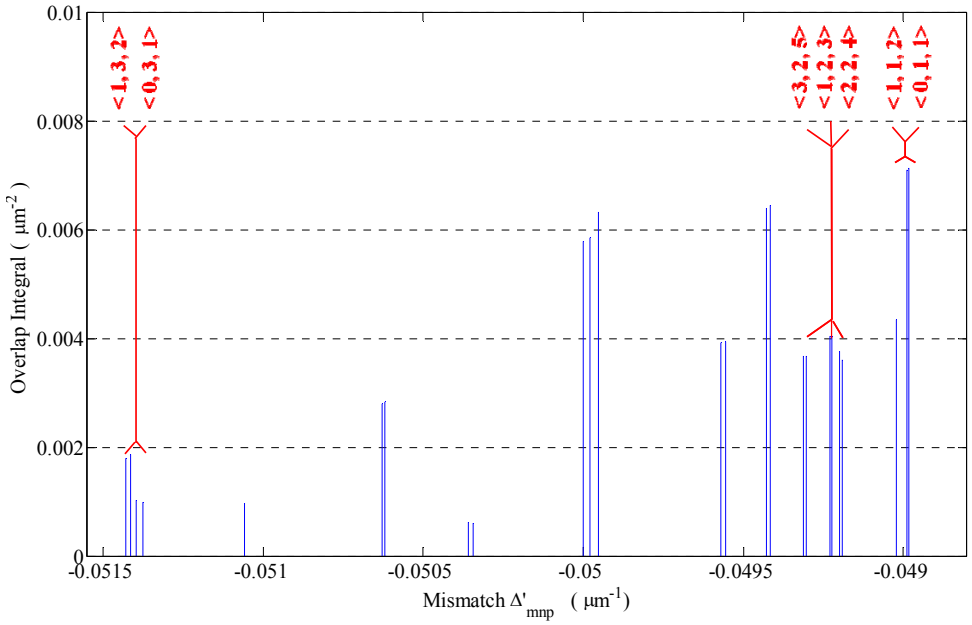

Figure 3-3 Interesting mode combinations corresponding to Case 1.

Table 3-1 Detailed information for potential Case 1 combinations

Signal mode m (1.54 μm)	Pump mode n (1.56 μm)	Sum-frequency mode p (0.775 μm)	Mismatch Δ'_{mnp} (μm^{-1})	Effective area A_{eff} (μm^2)	Difference between mismatches (μm^{-1})
0	1	1	-0.04898	140.33	3.85668E-05
1	1	2	-0.04902	229.83	
2	2	4	-0.0492	265.82	2.23745E-05
1	2	3	-0.04922	247.04	8.97802E-05
3	2	5	-0.04931	272.70	
0	3	1	-0.05134	1008.06	7.54053E-06
1	3	2	-0.05142	536.19	

3.3.2 Case 2

In the Case 2 scenario, two mode combinations $<m_1, n_1, p>$ and $<m_2, n_2, p>$ are simultaneously phase-matched, corresponding to the up-conversion of two different signal/pump mode pairs (m_1, n_1) and (m_2, n_2) to the same sum-frequency mode p. This means that, by adjusting the relative phases and magnitudes of the two pump modes n_1 and n_2, one can select for up-conversion any superposition of the two corresponding signal modes m_1 and m_2, without affecting the orthogonal superposition or any other modes. Case 2 can have applications as a dynamically reconfigurable spatial-mode de-multiplexer for both classical and quantum purposes. The quantum properties of the signal are preserved after the up-conversion process if its efficiency is close to 100%, and no other modes (unwanted processes) are coupled in. Figure 3-4shows all possible mode combination pairs and indicates promising Case 2 combinations (which have no neighbors) by red arrows.

Table 2 shows details for all promising Case 2 mode combinations. Each mode combination pair is composed of the two conjugate combinations $<m, n, p>$ and $<n, m, p>$, which are nearly degenerate in phase mismatch (the maximum difference of mismatch, 1.36×10^{-5}, indicates allowable nonlinear crystal length up to 31 mm). Each mode combination pair is well separated from other mode combinations, i.e., the unwanted processes are strongly suppressed. Note that by using periodic poling with two QPM periods, it might be possible to realize processes <1,3,0>, <3,1,0>, <0,2,0>, and <2,0,0> in the same waveguide, which enables the selective up-conversion of an arbitrary superposition of signal modes m = 0, 1, 2, 3. Another possibility is to use two poling periods to realize the processes <2,3,1>, <3,2,1>, <1,2,1>, and <2,1,1> in the same waveguide, enabling the selective up-conversion of an arbitrary superposition of signal modes m = 1, 2, 3.

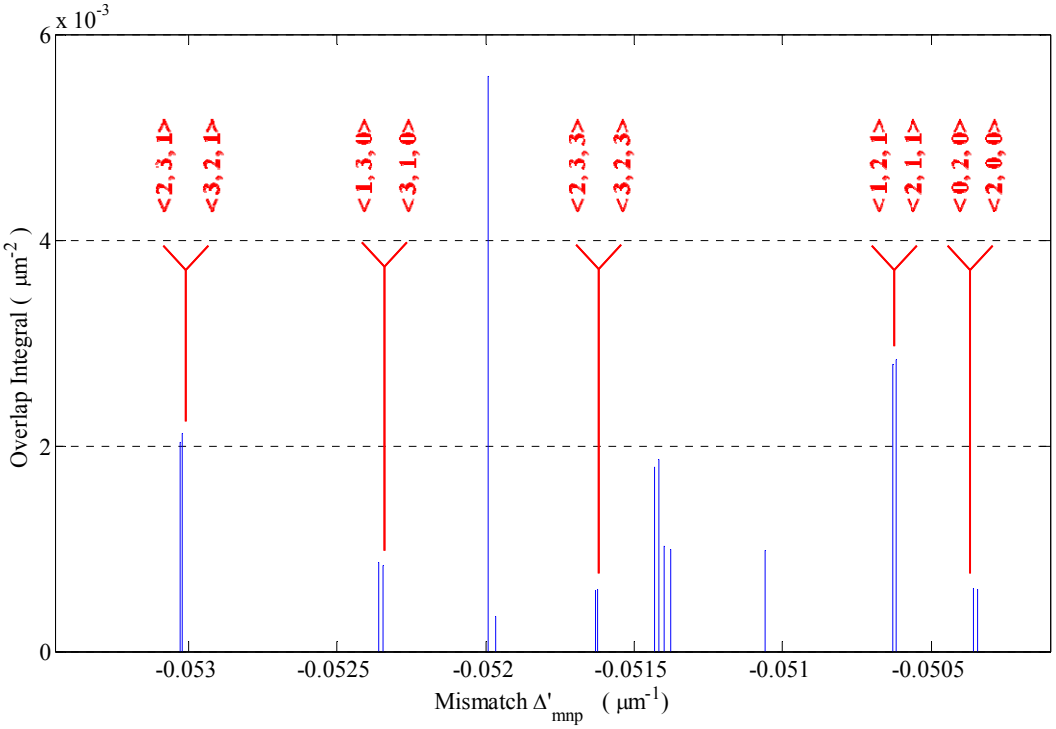

Figure 3-4 Interesting mode combinations corresponding to Case 2.

Table 3-2. Detailed information for potential Case 2 combinations

Signal mode m (1.54 μm)	Pump mode n (1.56 μm)	Sum-frequency mode p (0.775 μm)	Mismatch Δ'_{mnp} (μm^{-1})	Effective area A_{eff} (μm^2)	Difference between mismatches (μm^{-1})
2	3	1	-0.05302	490.44	1.35633E-05
3	2	1	-0.05303	472.37	
1	3	0	-0.05235	1153.40	8.31116E-06
3	1	0	-0.05236	1196.17	
2	3	3	-0.05162	1694.92	7.54053E-06
3	2	3	-0.05163	1652.89	
1	2	1	-0.05062	357.91	1.58517E-05
2	1	1	-0.05063	351.99	
0	2	0	-0.05034	1610.31	7.54053E-06
2	0	0	-0.05036	1647.45	

3.4 Conclusions

We have numerically analyzed two frequency up-conversion scenarios in a spatially-multimode PPKTP waveguide and proposed their application for classical and quantum information purposes. In the first scenario, a single pump mode can up-convert several different signal modes to different SFG modes, which is similar to an image up-conversion. In the second scenario, one pair of signal and pump modes is converted to an SFG mode and, at the same time, a different pair of signal and pump modes is up-converted to the same SFG mode. In the second scenario, by adjusting the relative phases and magnitudes of the two pump modes, one can select for up-conversion any superposition of the two corresponding signal modes without affecting the orthogonal superposition or any other modes, which can be used for spatial-mode demultiplexing in both classical and quantum communications. For a 20×6 μm^2 waveguide, we have found three potentially interesting mode combinations for the Case 1 and five interesting mode combinations for the Case 2.

Chapter 4

EXPERIMENTAL DEMONSTRATIONS

4.1 EXPERIMENTAL DEMONSTRATION OF SPATIAL-SELECTIVE FREQUENCY UP-CONVERSION IN $\chi^{(2)}$ MULTIMODE WAVEGUIDE

4.1.1 Introduction

Demultiplexing of spatial modes (e.g., those of a multimode fiber) is important for both classical and quantum communications, which evolve toward employing mode-division multiplexing to increase the channel capacity [30]. Moreover, dynamic reconfigurability of the demultiplexer's mode basis is highly desirable. In classical transmission, such reconfiguration could undo the mode mixing and reduce the required electronic processing of the received signal. In quantum key distribution, switching between mutually unbiased mode bases could increase the dimension of the Hilbert space used for encoding. In either case, low loss and low crosstalk of the demultiplexer are important.

In the preceding Section, based on our analysis of mode interaction in nonlinear waveguides [18], we have proposed the use of sum-frequency generation (SFG) in a multimode $\chi^{(2)}$ waveguide for selective up-conversion of the desired spatial mode of the signal, which nonlinearly interacts only with a specific spatial mode of the pump owing to quasi-phase-matching (QPM) conditions [15, 31]. In a waveguide with multiple QPM gratings, several different signal modes can be paired with the corresponding pump modes and consequently up-converted to the same SFG mode. Thus, by choosing a particular superposition of pump modes, one can up-convert (demultiplex from the input signal) any superposition of the signal modes in the given mode space, while all the orthogonal signal modes remain undisturbed and can be subsequently demultiplexed by another waveguide with a different pump profile. Theoretically, the SFG up-conversion efficiency can reach 100%, which makes it very attractive for applications where the

quantum state of the mode has to be preserved [32]. Mode couplings in the spontaneous parametric down-conversion process were previously observed in vertically-multimode PPKTP waveguides [6, 7]. However, because these waveguides had step-index profiles in the horizontal direction and erfc-function index profiles in the vertical direction, their mode profiles were very asymmetric and not well suited for matching to fiber modes.

In this following sections, we present proof-of-concept experiments demonstrating mode-selective up-conversion in a two-mode signal space, where the spatial profile of the pump, reconfigurable by a spatial light modulator (SLM), selects the desired signal-mode superposition to be up-converted. We employ a graded-index periodically poled lithium niobate (PPLN) waveguide, whose TM spatial modes have >98% overlap with free-space elliptic Hermite-Gaussian modes and can be easily matched to multimode fiber modes. The obtained high internal conversion efficiencies, as well as low crosstalk, indicate potential of this approach for both classical and quantum demultiplexing applications.

4.1.2 Experimental configuration

The experimental setup is shown in Fig. 4-1. The signal (1540 nm) and pump (1560 nm) are carved into 400-ps-long flat-top pulses with a 20-MHz repetition rate by a high-extinction-ratio electro-optic Mach-Zehnder modulator (EOSpace). After a high-power erbium-doped fiber amplifier the pulses enter free space through a fiber collimator. The signal and pump beams are then separated by a dichroic beam splitter (DBS), phase-modulated by two separate regions of the same 512×512 SLM (Meadowlark Optics), and recombined by another DBS. 180° prisms on translation stages are used for temporal alignment of the pulses. By using $\pm\theta$ checkerboard SLM pattern (where θ varies slowly across the checkerboard) along with a low-pass spatial filter in a 4f lens system, the phase modulation of the SLM is converted to amplitude modulation $\sim\cos(\theta)$. The 4f achromatic doublet system is followed by an aspheric lens for focusing the beams into the

waveguide, so that the SLM plane corresponds to the Fourier plane of the waveguide face. The 52-mm-long PPLN waveguide supports two TM modes in 1550 nm region and has a QPM grating with 16.1-μm period designed to nonlinearly couple TM_{00} signal and TM_{01} pump (as well as TM_{01} signal and TM_{00} pump) to TM_{01} mode of SFG at 775 nm [25, 26]. At the PPLN output, the signal, pump, and SFG beams are separated and monitored by cameras, power meters, fast detectors, and an optical spectrum analyzer (OSA).

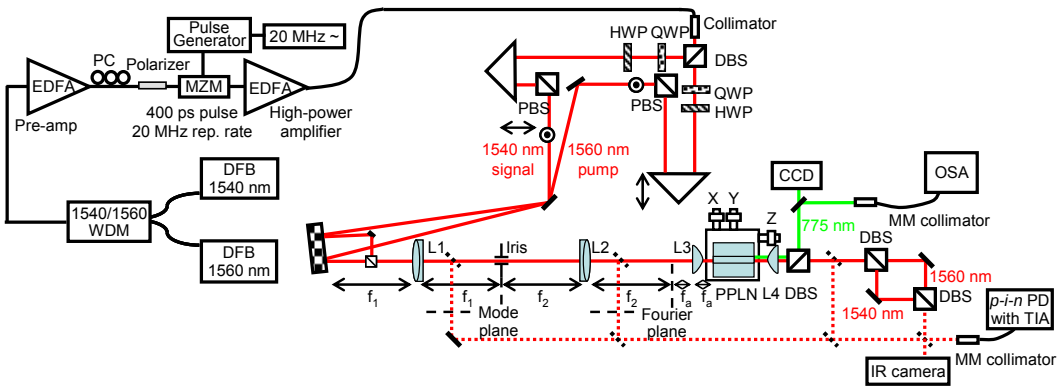

Figure 4-2 Experimental setup for selective up-conversion.
DFB–distributed feedback laser, MZM–Mach-Zehnder modulator, DBS–dichroic beam splitter, PBS–polarization beam splitter, EDFA–erbium-doped fiber amplifier, HWP–half-wave plate, QWP–quarter-wave plate, OSA–Optical spectrum analyzer.

4.1.3 Two-mode PPLN waveguide specification

In the chapter 3, we designed a PPKTP channel waveguide which supports four propagating modes at 1550 nm. Due to the limited fabrication technology to achieve such four-mode PPKTP, a two-mode PPLN waveguide, instead, has been fabricated by our collaborators from Stanford University (Prof. M. Fejer's group). Figure 4-3 shows the mode profile of signal, pump, and SFG modes. Based on the Figure 4-4 (top), the optimum waveguide width is 12.5 μm where the desired mode combination and undesired mode combination are well separated, while the phase-matching curve has almost flat slope for the desired mode combination, i.e., is very tolerant to fabrication imperfections. Note that the waveguide width below 10 μm is not desirable

due to the low fabrication tolerance (meaning high sensitivity to fabrication inaccuracy) even though it has large QPM period separation between desired / undesired mode combination.

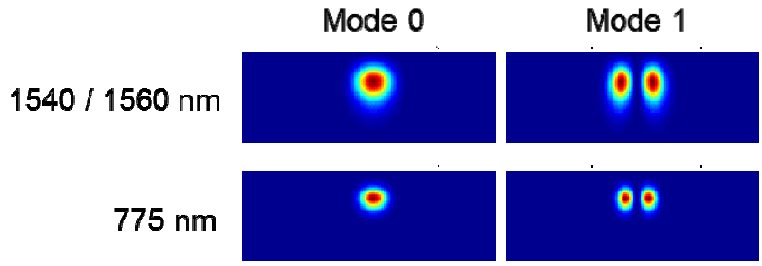

Figure 4-3 Mode profiles of two-mode PPLN waveguide (courtesy of C. Langrock, Stanford Univ.)

From the Figure 4-4(top), we can decide the optimum parameter as 16.1 μm QPM period, 1.7 μm (depth), and 12.5 μm (width). The Figure 4-4 (middle) shows minimum required length of the PPLN waveguide to separate desired and closest undesired mode combinations at 12.5 μm width. In other words, the minimum PPLN waveguide length (lower bound) that introduces phase mismatch to the undesired mode combination (blue line of Figure 4-4) not to the desired combination is 5 mm. If we increase waveguide length more than 5 mm, undesired mode combination will lose phase matching quickly, yielding low SFG conversion efficiency, whereas phase matching for the desired mode combination is maintained, resulting in high SFG conversion efficiency. By simple calculation, the SFG power difference between desired mode and closest mode combination for the waveguide length of 50 mm will be ~100 times because to the first order the SFG power is proportional to the square of the effective interaction length. Figure 4-4 (bottom) shows the maximum PPLN waveguide length for simultaneous phase matching between two desired mode combination. Note that even though these two mode combinations are almost degenerate, there is still small amount of phase mismatch limiting available waveguide length. At 12.5 μm width, the maximum PPLN waveguide length (upper bound) is ~ 1 m but, in practice, a few centimeter waveguide is still enough to achieve good conversion efficiency. Based on the three modeling graphs from the Figure 4-4, the theoretical optimum waveguide specifications are

1.7 μm (D) × 12.5 μm (W) ×52 mm (L) with 16.1 μm QPM period. However, we found that the width of 11 μm has better measured performance, and this is the actual width used for our experiment.

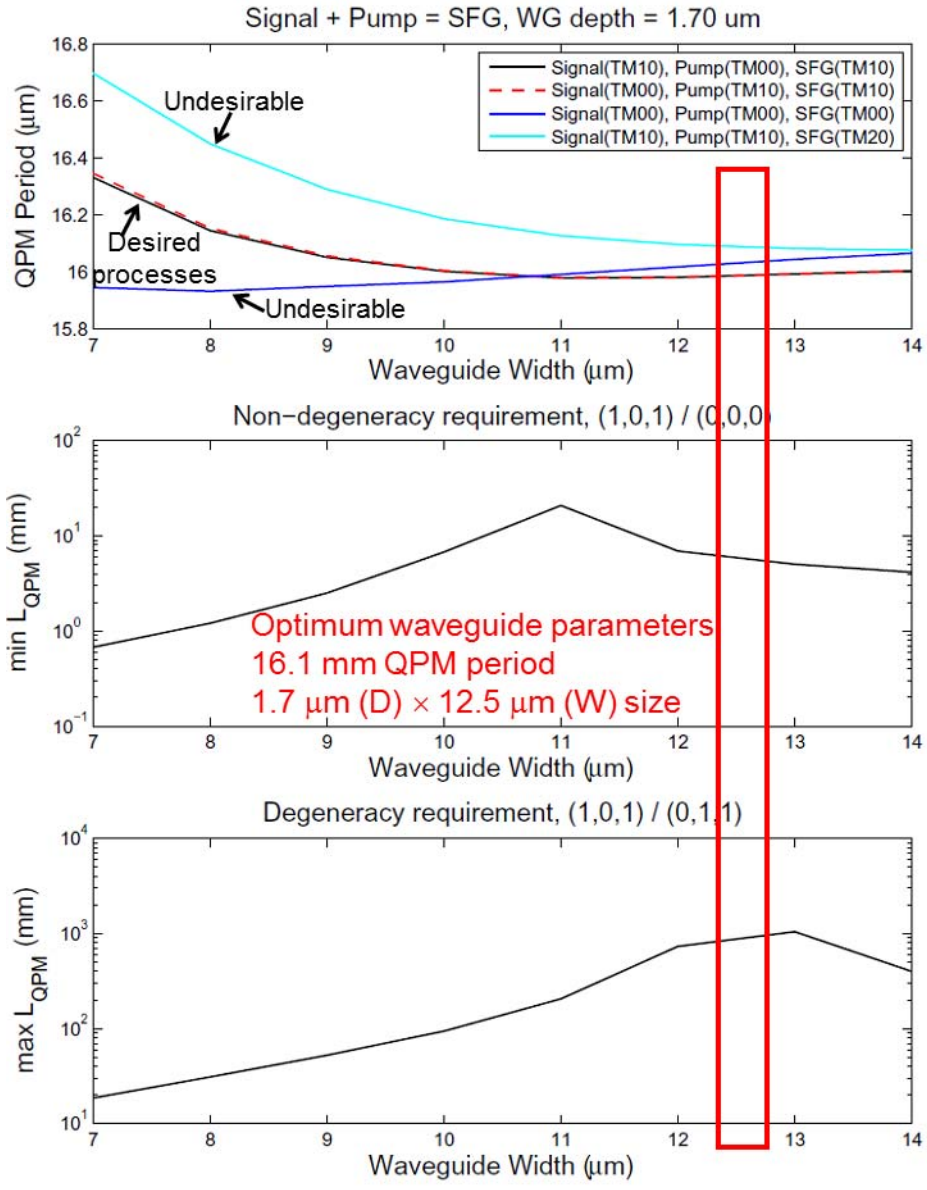

Figure 4-4 Optimum waveguide parameters (courtesy of C. Langrock, Stanford University)

The Figure 4-5 is the measured phase-matching temperature graph for the case of $TM_{00,signal} + TM_{01,pump} \rightarrow TM_{01,SFG}$. Note that the temperature curve is asymmetric rather than symmetric. Our best speculation is that this asymmetric curve is caused by the uneven heat distribution to PPLN waveguide surface. For example, the waveguide is placed in aluminum-based waveguide holder with PID temperature controller, and a thermal paste (Artic-silver) is used for good heat transfer between the aluminum holder and the PPLN waveguide. If the thermal paste is not applied evenly, the heat distribution could be uneven.

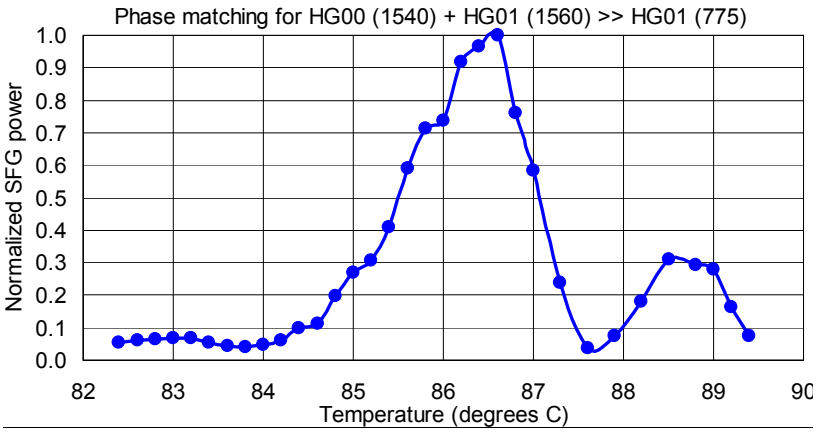

Figure 4-5 temperature vs normalized SFG power

4.1.4 400-ps optical pulse generation

The nonlinear optical interaction responds to peak power rather than average power. For this purpose, 400-ps-long optical pulse with 20 MHz repetition rate is generated with electric pulser and high-extinction-ratio (> 45dB) electro-optic modulator as shown in Figure 4-6. Without pre-amplifier, maximum 7-dBm output power from TLS experiences ~ –7 dB insertion loss and ~20 dB power reduction due to 1/125 duty cycle from EO modulator and does not reach the minimum input power of high power EDFA. For this purpose, pre-amplifier is used, giving output

power of 23 dBm. In addition to pre-amplifier, high-extinction-ratio EO modulator is used both to minimize amplified spontaneous emission (ASE) noise and to maximize peak power. Minimizing ASE noise is especially important for the single-photon-level experiment.

The polarization need to be controlled, because EO modulator responds only to vertical polarization. Our EO modulator has low damage threshold of ~ 10 mW average power due to the thin film used to filter out cross polarization (horizontal polarization). Because the output power from pre-amplifier is 23 dBm, the fiber polarizer is used to protect the EO modulator during the process of optimizing the polarization with polarization controller.

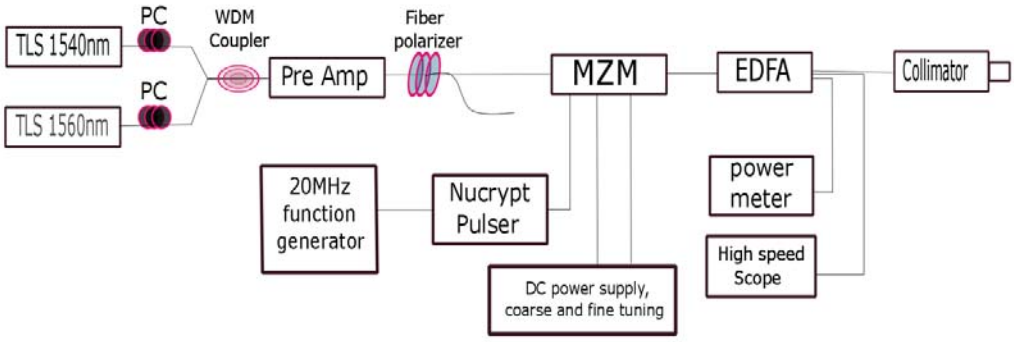

Figure 4-6 Optical pulse generation with electrical pulser and high-extinction-ratio electro-optical modulator

4.1.5 Complex modulation of spatial modes

We used 512×512 phase-only reflective spatial light modulator (SLM) for complex modulation of spatial modes. The 2×2 or 4×4 super-pixels interfere in mode plane and selecting only fundamental diffraction order by iris results in complex modulation (see Figure 4-2 and Figure 4-7). The fundamental guiding mode of PPLN waveguide has 1/*e* intensity radius of a_{0x}=2.67 μm, a_{0y}=1.58 μm. Then, the mode size in the SLM plane is expressed as Eq. (3.1), where f_a, f_1, f_2 are effective focal length of aspherical lens and lens for telescope configuration with values of 6.24 mm, 200 mm, and 250 mm, respectively.

$$a_{x,y(SLM)} = \frac{f_a f_1}{f_2} \frac{\lambda}{2\pi a_{x,y(WG)}} \tag{3.1}$$

Once we know the desired mode size in the SLM plane, we can generate checkerboard pattern according to Eq. (3.2). The radius of the incident beam to SLM is measured by knife-edge method ($a \approx 1.02\ mm$) and desired beam is modeled as Hermite-Gaussian mode with radius calculated from Eq. (3.1).

$$\frac{\tilde{E}_{\text{desired}}(x,y)}{\tilde{E}_{\text{incident}}(x,y)} = \cos(\theta)\exp(i\phi) \tag{3.2}$$

The code for the checkerboard pattern is written with Matlab which generates 24-bit BMP image files for SLM.

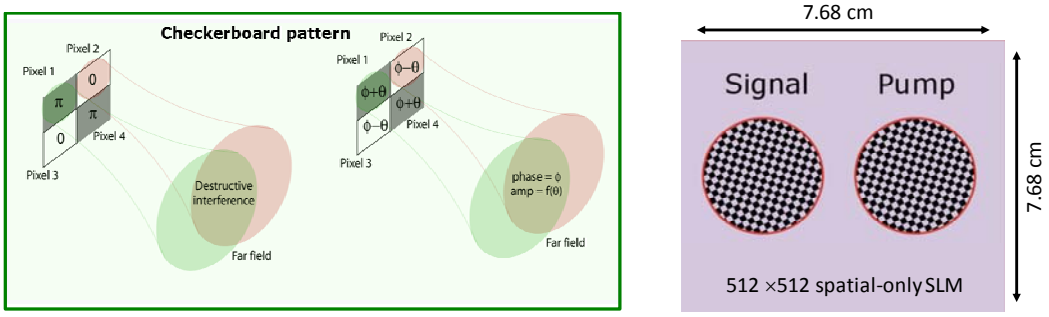

Figure 4-7 (left) Checker-board pattern with 2 phase values, (right) locations of signal and pump on the surface of SLM

The phase-modulated images after telescopic lens (Fourier plane with respect to the waveguide face) are shown in Figure 4-8.

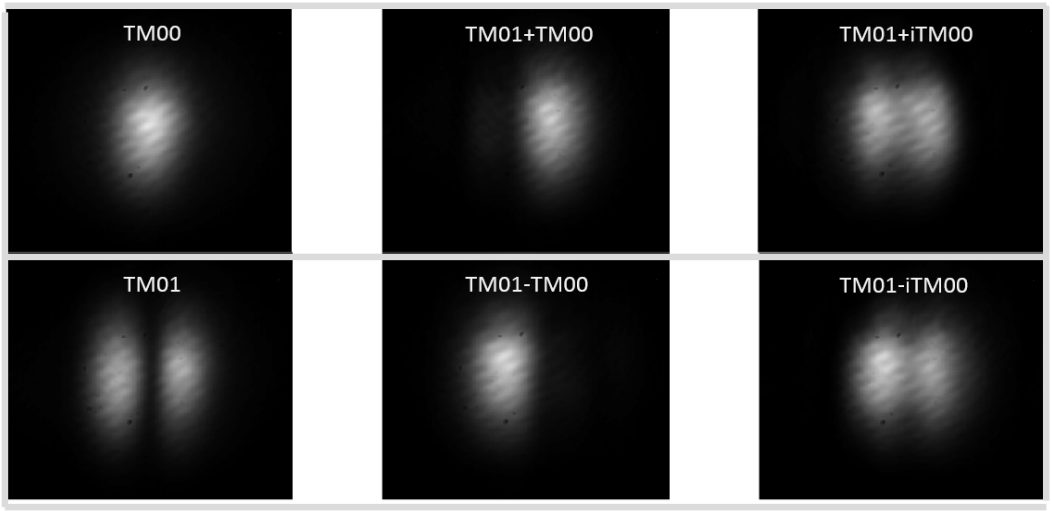

Figure 4-8 Complex modulated spatial modes after telescopic lens measured by IR CCD camera

4.1.6 Results / Discussion

Figure 2 and Table 1 present the measurement results. We define the internal photon conversion efficiency as $\eta_{int} = 1 - d$, where d is the signal depletion coefficient given by the ratio of the output signal powers with and without the pump. We define the external photon conversion efficiency η_{ext} as the ratio of one-half of the output SFG power to the signal power before the waveguide, i.e., it includes coupling and waveguide propagation losses. The up-conversion of the 1540-nm signal modes TM_{00}, TM_{01}, TM_{01}–TM_{00}, or $TM_{01}+iTM_{00}$ is achieved by pumping the PPLN with 1560-nm modes TM_{01}, TM_{00}, TM_{01}–TM_{00}, or $TM_{01}+iTM_{00}$, respectively (0.8–2.7 W peak power range), and yields $\eta_{int} \geq 70\%$ in all cases. The crosstalk, defined as the inverse of the ratio of η_{ext} values for the desired signal mode and the undesirable orthogonal mode, is better than –16 dB in all cases. The η_{ext} values for the up-conversion of the superposition modes are lower than those for up-conversion of TM_{00} and TM_{01} modes because we used different SLMs in these two experiments, and the SLM in the superposition case generated mode profiles with lower

extinction ratio, degrading the coupling efficiency. A better SLM would be expected to yield $\eta_{ext} >$ 50% for all cases.

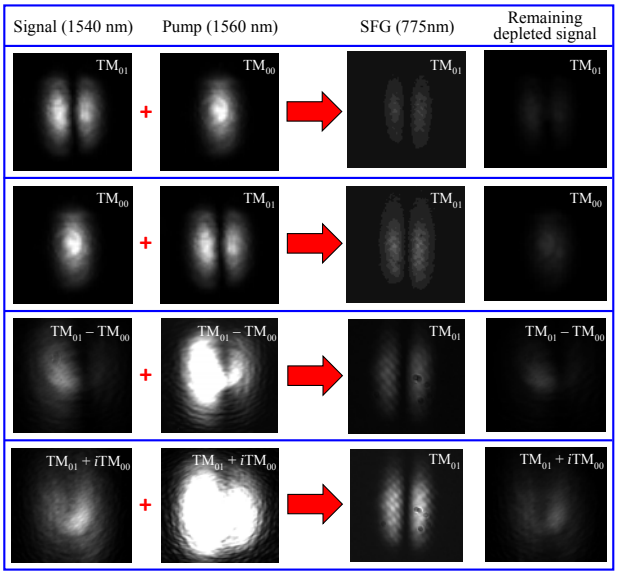

Figure 4-9 Spatial profiles of the signal, pump, and SFG beams

Table 4-1. internal and external photon conversion efficiency and crosstalk

signal	pump	η_{int}	η_{ext}	crosstalk
TM_{00}	TM_{00}	1.8%	1.1%	–16.4 dB
TM_{01}	TM_{00}	87%	48%	
TM_{00}	TM_{01}	80%	26%	–18.1 dB
TM_{01}	TM_{01}	0.06%	0.4%	
$TM_{01} + TM_{00}$	$TM_{01} - TM_{00}$	0.74%	0.16%	–20.2 dB
$TM_{01} - TM_{00}$	$TM_{01} - TM_{00}$	70%	16.7%	
$TM_{01} + iTM_{00}$	$TM_{01} + iTM_{00}$	70.6%	15.1%	–20.3 dB
$TM_{01} - iTM_{00}$	$TM_{01} + iTM_{00}$	1.2%	0.14%	

4.1.7 Conclusions

To summarize, we have experimentally demonstrated frequency up-conversion of selected spatial modes and mode superpositions of a two-mode PPLN waveguide with ≥70% internal conversion efficiency and better than –16 dB mode crosstalk. The mode selection is done by choosing the pump spatial profile, which can be reconfigured by an SLM at up to a ~50 Hz rate. With several QPM gratings, mode-selective up-conversion can be extended to a larger mode space and used for dynamically reconfigurable mode demultiplexing of classical and quantum signals.

4.2 EXPERIMENTAL DEMONSTRATION of 2×10.7 Gb/s NRZ spatial-mode demultiplexing by mode-selective SFG

4.2.1 Introduction

The all-optical reconfigurable spatial-mode de-multiplexing for MDM system is one of our proposed applications, where each spatial mode works as an independent communication channel, directly increasing information capacity. To properly evaluate our PPLN waveguide as a function block for the spatial-mode de-multiplexer for high-speed fiber communication, we compare the performances between data-modulated single-mode signal (only the desired mode) and data-modulated two-mode signals (one desired mode + one undesired mode). We measure both eye-diagram and bit-error-rate and demonstrate that our low crosstalk performance is sufficient to sort out one signal mode with the price of ~ 2.5 dB power penalty due to crosstalk for 10.7 Gb/s non-return-zero (NRZ) on-off-key (OOK) modulated signal.

4.2.2 Experimental configuration

Figure 4-10 shows experimental configuration, which is similar to our previous experimental setup, but with distributed feedback (DFB) laser used instead of TLS laser to make two signal modes mutually incoherent. In other words, since the two signal modes work as independent communication channels, we make the two signals from the same DFB laser source and use 1 km of SMF delay between them (much longer than the 50-m coherence length of the DFW laser source with linewidth of ~ 4 MHz) to ensure random phase between the two spatial modes. In addition to DFB laser, NRZ EO modulator from JDSU is used for 10.7 Gb/s data modulation instead of high-extinction-ratio EO modulator.

The two signal spatial modes are obtained by combining two signal polarizations (the SLM modulates only vertical polarization and merely reflects the horizontal) with a half-wave plate immediately before the aspheric lens at the waveguide entrance. The waveguide only

supports vertically-polarized (TM) modes and thus serves as a polarizer onto which the half-wave plate projects the superposition of the two modes.

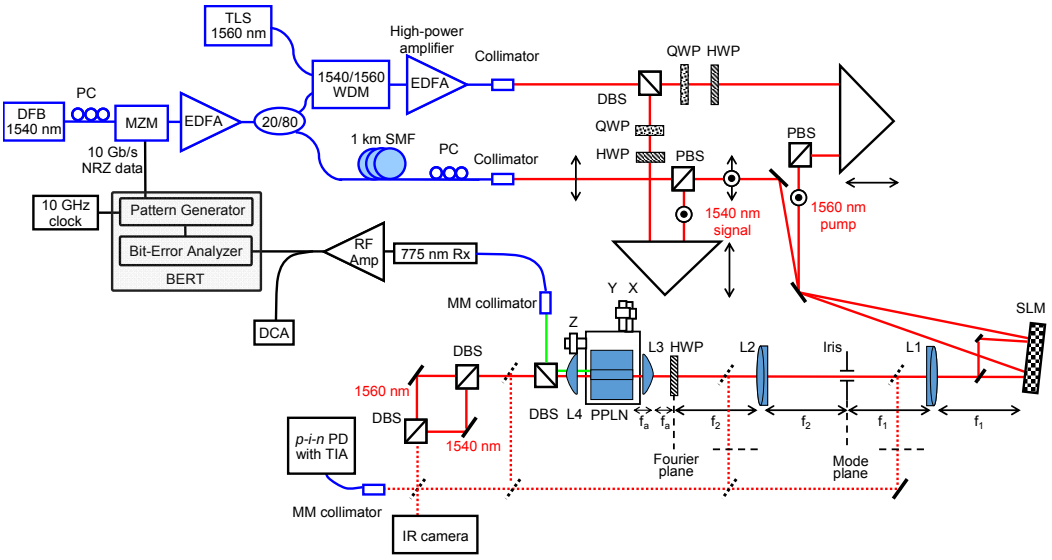

Figure 4-10 Experimental setup with 10GHz NRZ signal
MZM: Mach-Zehnder modulator; PC: polarization controller; WDM: wavelength-division-multiplexing coupler; HWP: half-wave plate; QWP: quarter-wave plate; PBS: polarization beam splitter; DBS: dichroic beam splitter; SLM: spatial light modulator; DCA: digital communication analyzer; PD: high-speed photodiode; TIA: transimpedance amplifier; Rx: 10 Gb/s photoreceiver; BERT: bit-error tester; SMF: single-mode fiber. Lenses L1 and L2 are achromatic doublets, lenses L3 and L4 are aspheric.

4.2.3 Results / Discussion

The external conversion efficiency for TM_{01} signal is 11% with –19.5 dB crosstalk, and the external conversion efficiency for TM_{00} signal is 7.7% with –20.7-dB crosstalk. Figure 4-11 shows the eye diagrams for back-to-back 1540-nm transmission (left), as well as for up-converted 775-nm signals without (middle) and with (right) the presence of the crosstalk from the data encoded into the second spatial mode of the 1540-nm signal. The measured BER versus received 775-nm power curves are shown in Figure 4-12, demonstrating that the presence of a second data-carrying

mode introduces only a moderate power penalty of 2–2.5 dB at bit-error-rate level of 10^{-9}, owing to the crosstalk in the SFG process.

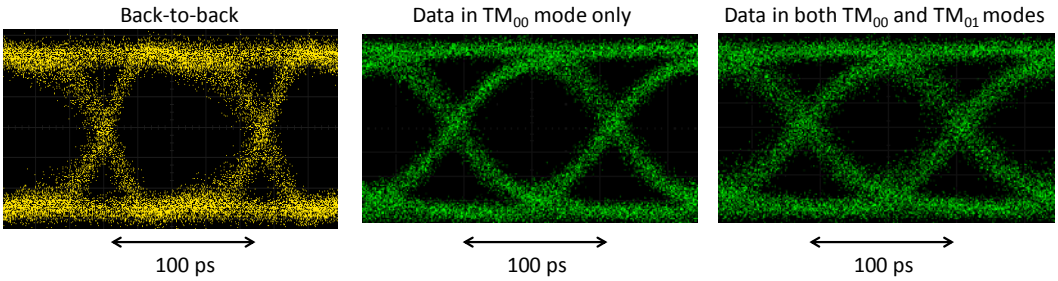

Figure 4-11 Eye diagrams.
Eye diagrams of the (left) back-to-back 1540-nm signal (output of the MZM), (middle) up-converted 775-nm signal originally encoded into 1540-nm TM_{00} mode only, (right) up-converted 775-nm signal originally encoded into 1540-nm TM_{00} mode, in the presence of crosstalk from the 1540-nm signal carrying data in TM_{01} mode. Note that the electrical bandwidth of the 1550-nm receiver (15 GHz) is wider than that of the 775-nm receiver (9 GHz).

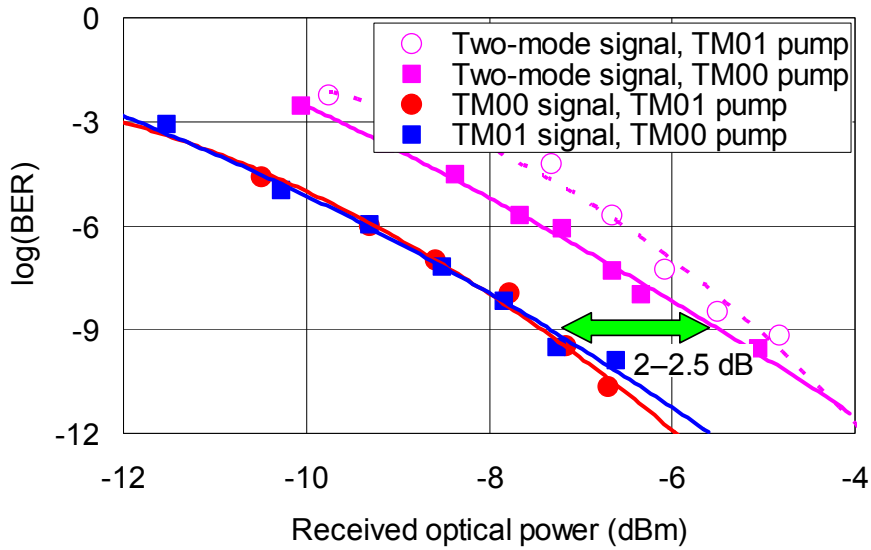

Figure 4-12 Bit-error-rate versus received SFG optical power for the cases of up-converting single-mode signals (red and blue) and of up-converting one mode of a two-mode signal (purple).

4.2.4 Conclusions

We experimentally demonstrated reconfigurable all-optical demultiplexing with two signal modes which are data-modulated in NRZ format with 10.7 GHz bandwidth. Two signal channels show a moderate 2.5 dB power penalty compared to a single signal channel, proving that our device can be used as a practical spatial mode de-multiplexer.

4.3 EXPERIMENTAL DEMONSTRATION OF MODE-SELECTIVE FREQUENCY UP-CONVERSION WITH A FEW-MODE-FIBER

4.3.1 Introduction

The practical spatial-division multiplexing (SDM) fiber-optic communication system is highly likely to be implemented on hybrid fiber comprising multiple few-mode fiber cores to maximize information capacity. For spatial-mode de-multiplexing of modes from a few-mode-fiber (FMF), it is important to test whether our PPLN waveguide-based de-multiplexer is compatible with LP modes of a few-mode-fiber. Here we perform prove-of-concept experiment of selective mode-conversion with OFS 6-mode fiber. Because the first two modes, LP_{01} and LP_{11}, of the FMF are similar to PPLN waveguide modes, we focus only on these two modes. This experiment can be expanded into higher-order modes of the FMF using a mode converter.

4.3.2 Experimental configuration

In this experiment we verify that the mode-selective frequency up-conversion is capable of demultiplexing the signals after propagation in 1-km of OFS 6-mode fiber. For that demonstration, we have assembled the setup shown in Fig. 4-13. Here, the original 1540-nm signal is split into two arms, one of which is spatially modulated by a phase plate shifting the phase of half-plane of the wavefront by π (this is used to excite mode LP_{11} of the fiber). The two arms are subsequently recombined and launched into the few-mode fiber (FMF). Output of the fiber goes through a 2:1 vertical beam expander to convert circular Gaussian modes of the FMF into elliptical Gaussian modes of the PPLN waveguide. 3-paddle polarization controller in the FMF is used to align the output LP_{11} mode, excited by the input TM_{01} mode, with horizontally-oriented TM_{01} mode of the waveguide.

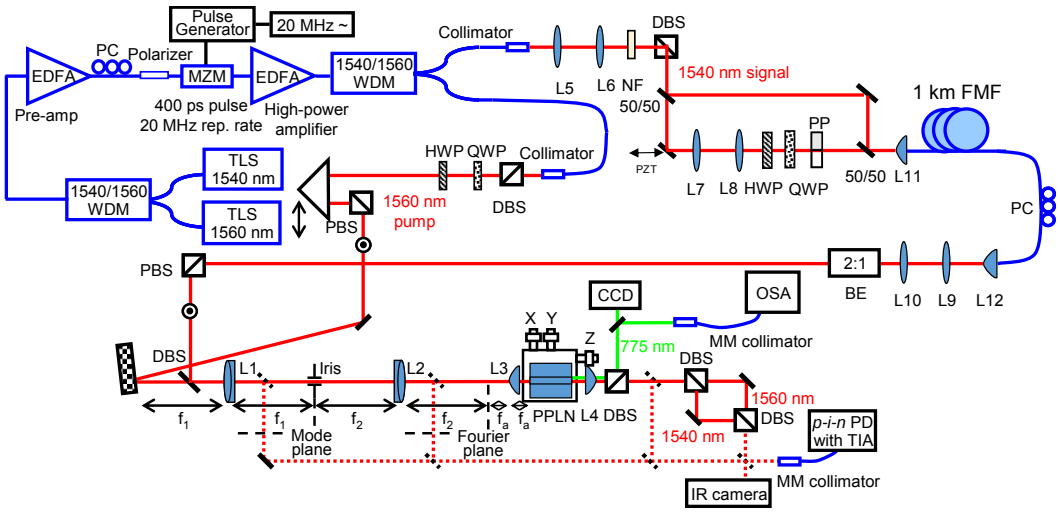

Figure 4-14 Experimental setup for a FMF

MZM: Mach-Zehnder modulator; PC: polarization controller; WDM: wavelength-division-multiplexing coupler; HWP: half-wave plate; QWP: quarter-wave plate; PP: phase plate; PBS: polarization beam splitter; DBS: dichroic beam splitter; SLM: spatial light modulator; NF: neutral-density filter; BE: 2:1 vertical beam expander; PD: high-speed photodiode; TIA: transimpedance amplifier; OSA: optical spectrum analyzer; FMF: few-mode fiber. Lenses L1 and L2 are achromatic doublets, lenses L3, L4, L11, and L12 are aspheric.

4.3.3 Results / Discussion

The measurement results are shown in Table 3, indicating greater than 46% internal conversion efficiencies and better than –14-dB crosstalk in de-multiplexing the spatial modes TM_{00} and TM_{01} after propagation in 1-km FMF.

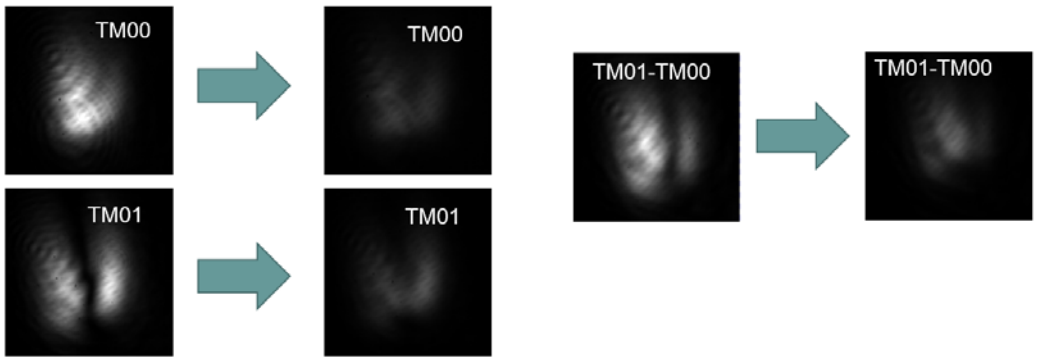

Figure 4-15 image of signal mode depletion (Fourier plane)

Table 4-2 Internal and external photon conversion efficiencies η_{int} and η_{ext} and crosstalk for frequency conversion after propagation in 1 km of FMF

Signal	Pump	Internal Conversion eff.	External conversion eff.	crosstalk
TM00	TM01	75%	23 %	-18 dB
TM01	TM01	0.51 %	0.37 %	
TM01	TM00	64.15%	13.4 %	-14.5 dB
TM00	TM00	0.3%	0.48 %	
TM01-TM00	TM01-TM00	46.3 %	20.5 %	-17.9 dB
TM01+TM00	TM01-TM00	0.6 %	0.33 %	

4.3.4 Conclusions

The mode-selective up-conversion of FMF modes is experimentally demonstrated. We obtained more than 46% of internal conversion efficiency with better than –14dB crosstalk. The main reason of performance degradation is due to mode-size mismatch among FMF modes, waveguide modes, and mode from collimator for pump. These things can be easily improved using higher-quality optics.

4.4 SINGLE-PHOTON-LEVEL MODE-SELECTIVE FREQUENCY-UP-CONVERSION IN MULTIMODE WAVEGUIDE

4.4.1 Introduction

Massively multimode quantum states represent an important resource for quantum information applications. For example, employing many temporal, polarization, and spatial modes of the fiber could dramatically increase the quantum key distribution (QKD) rates for a given link distance. This can be achieved either by using each mode as a separate quantum channel, or by using many modes to create encoding in a high-dimensional Hilbert space. A critical enabling element for either of these two approaches is a low-loss mode de-multiplexer, with the latter approach additionally requiring from the de-multiplexer an ability to dynamically switch between mutually unbiased bases. One attractive technology that can be used for such mode de-multiplexing is the quantum frequency conversion (QFC) from infrared to visible via sum-frequency generation (SFG) [2], which also can be used to interface the photonic qubits or qudits with atomic memory and to avoid large dark counts of the infrared single-photon detectors. The use of QFC for de-multiplexing and lossless shaping of temporal waveforms has been extensively investigated [3, 4, 33]. For spatial modes, we have recently proposed [15, 31] and experimentally demonstrated [34] a dynamically reconfigurable spatial-mode demultiplexer based on quasi-phase-matching (QPM) in a multimode periodically-polled lithium niobate (PPLN) waveguide. By tailoring the QPM conditions, the desired signal mode can be made to nonlinearly interact with a specific spatial mode of the pump. In a waveguide with multiple QPM gratings, several different signal modes can be paired with the corresponding pump modes and consequently up-converted to the same SFG mode. By choosing a particular superposition of pump modes, one can up-convert (demultiplex from the input signal) any superposition of the signal modes in the given mode space, while all the orthogonal signal modes remain undisturbed and can be subsequently demultiplexed in another waveguide by a different pump profile. In theory, one can achieve 100% up-conversion, which

makes the SFG very attractive for applications where the quantum state of the mode has to be preserved [32]. Mode couplings in the spontaneous parametric down-conversion process were previously observed in vertically-multimode PPKTP waveguides [6, 7]. These waveguides had step-index profiles in the horizontal direction and erfc-function index profiles in the vertical direction, which made their mode profiles very asymmetric and not well suited for matching to fiber modes. In previous Sections, we employed a graded-index PPLN waveguide, whose modes had >98% overlap with multimode-fiber modes, and experimentally demonstrated mode-selective up-conversion of either TM_{00} or TM_{01} mode, or any of their superpositions from 1540 nm into TM_{01} mode at 775 nm. Because this demonstration was done with classical (μW level) signal beams, it remained to be seen whether this method could work with quantum states, where a few parasitic effects (Raman scattering in the PPLN, second-harmonic generation of the pump, broadband noise of the pump beam, etc.) might prevent operation with single-photon-level signals.

Hence, in this Section we extend our work into the single-photon regime and demonstrate mode-selective up-conversion with high conversion efficiency, low crosstalk, and sufficient suppression of the parasitics.

4.4.2 Experiment configuration

Our experimental setup adopted to quantum measurements is shown in Fig. 4-16. The signal (1540 nm) and pump (1560 nm) are carved into 400-ps-long flat-top pulses with a 20-MHz repetition rate, separated in free space by a dichroic beam splitter (DBS), modulated by two separate regions of the same 512×512 spatial light modulator (SLM), recombined by another DBS, and coupled into a 52-mm-long PPLN waveguide that supports two TM modes in 1550 nm region. The waveguide's QPM grating is designed to nonlinearly couple TM_{00} signal and TM_{01} pump (as well as TM_{01} signal and TM_{00} pump) to TM_{01} mode of SFG at 775 nm [25]. At the PPLN output the

signal, pump, and SFG beams are separated, and the SFG photons are counted by a Perkin-Elmer SPCM-AQRH-13-FC single-photon detector.

To enable measurements at the single-photon level, we first suppress amplified spontaneous emission (ASE) noise of the pump beam at the signal wavelength by a combination of a 1560-nm reflecting bandpass filter (BPF) and a two-stage 1540-nm notch filter (NF), both based on volume Bragg gratings (VBGs from Optigrate). After separating the SFG from the signal and pump by a DBS and a dispersive prism, we suppress a small amount of strongly phase-mismatched second harmonic of the pump at 780 nm by several 3-nm-wide BPFs centered at 775 nm, and further eliminate Raman scattering and ASE outside of the up-converted signal bandwidth by a 0.035-nm-wide VBG-based 775-nm-reflecting BPF. We attenuate the input 1540 nm signal so that it has average photon number of ≈ 0.1 per pulse at the output of the PPLN waveguide. When the signal is turned off (but the pump is kept on), the SFG photon counts drop by more than two orders of magnitude, indicating > 10^2 ratio of signal to background noise photons.

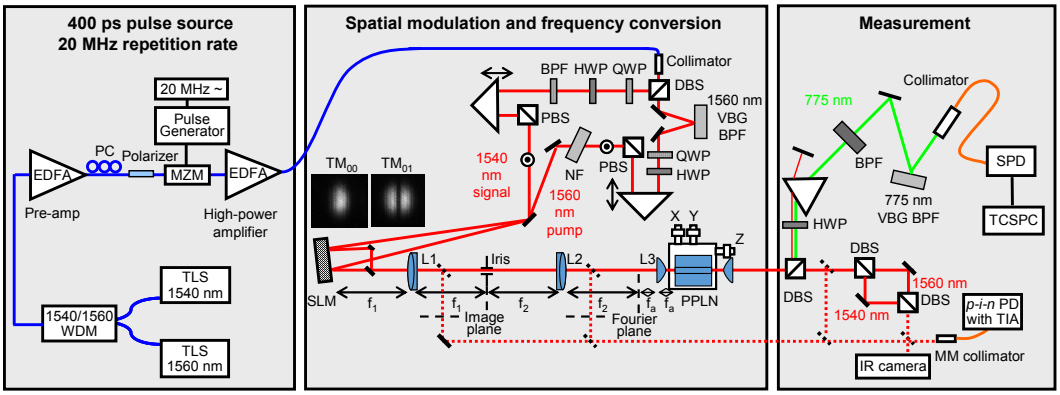

Figure 4-17 Experimental setup for single-photon-level selective up-conversion. TLS–tunable laser source, MZM–Mach-Zehnder modulator, DBS–dichroic beam-splitter, PBS–polarization beam-splitter, EDFA–erbium-doped fiber amplifier, HWP–half-wave plate, QWP–quarter-wave plate, BPF–bandpass filter, NF–notch filter, VBG–reflecting volume Bragg grating, SLM–spatial light modulator, SPD–single-photon detector, TCSPC–time correlated single-photon counter. The insert shows the profiles for signal/pump TM_{00} and TM_{01} modes in Fourier plane.

4.4.3 Filter characterizations

For the proper quantum measurement, we need to identify parasitic noises and suppress the noises. First of all, we need to suppress 1540-nm signal ASE from the pump path to a level << 0.1 photon/pulse. The 0.1 photon/pulse is corresponding –96 dBm average signal power p, because $p = h\nu \times (0.1 \text{ photons/pulse}) \times (2 \times 10^7 \text{ pulses/s}) \approx$ -96 dBm .. To suppress the 1540-nm ASE noise from the pump path, we used three DBSs (1540nm/1560nm), two 1540-nm VBG notch filters (NF), and a reflective VBG-based 1560-nm BPF. The two DBSs suppress 1540-nm ASE by >30 dB (i.e., by 15 dB each), and two notch filters suppress it by > 80 dB, as shown in the Figure 4-18. The 0.8-nm-wide reflective VBG 1560-nm BPF suppresses 1540-nm ASE by another ~20 dB, simultaneously suppressing the rest of the broadband ASE noise. Figure 4-18 (left) is expressed regarding relative power with only pump power on. The absolute signal power is approximately 10 dB lower than the absolute pump power due to EDFA gain slope. In worst case scenario of 1 W pump power, the 1540-nm signal ASE after suppression by filters is 30 dBm – 10 dB (from the difference between pump and signal power) – 145 dB (from filters) = –125 dBm, which is << –96 dBm. It shows that the 1540-nm signal ASE is a lot smaller (~ 30 dB) than 0.1 photon/pulse level.

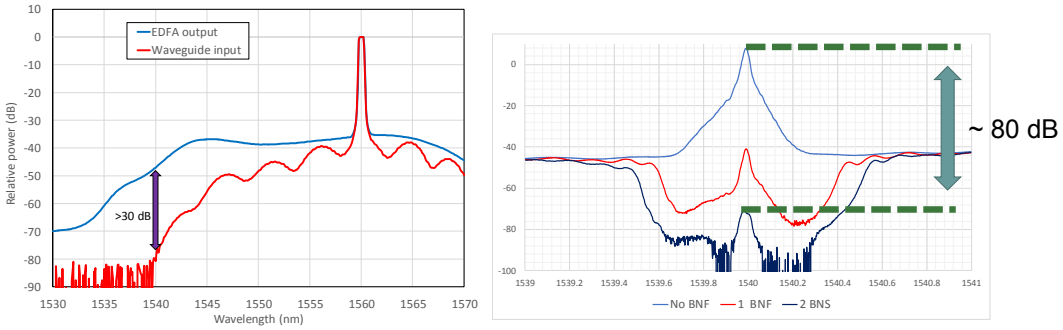

Figure 4-18 (left) Characterization two DBS filters. (right) Characterization of Bragg-grating notch filters..

The next thing to consider is the suppression of second harmonic generation (SHG) contributed by the pump. Figure 4-19 shows measurement with the case of (left-top) both of signal (before attenuation by ND filters) and pump, (left-middle) signal power only, (left-bottom) pump

power only, and (right) both signal and pump power but with a 3-nm-wide 775-nm BPF from Semrock. As shown in the Figure 4-19, the SHG is suppressed by ~35 dB with a single 775nm BPF. The measured absolute SHG of the pump is ~ 2 μW (–27 dBm), and we apply three 775-nm BPF (105 dB of suppression) to ensure the suppression of SHG to << 0.1 photon/pulse level.

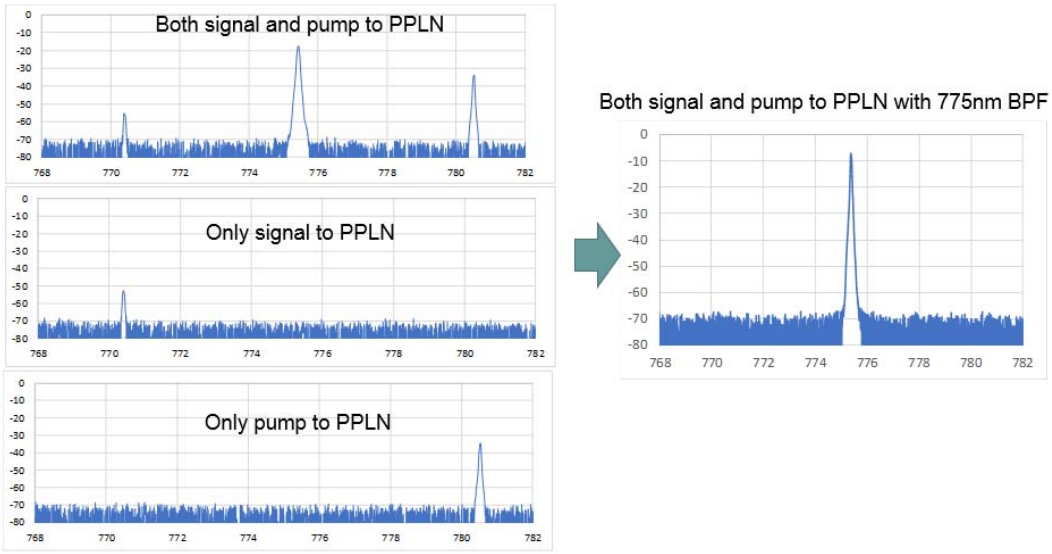

Figure 4-19 Suppression of SHG by 0.8-nm-wide BPF centered at 775 nm

Finally, we need to minimize unwanted Raman scattering noise generated due to high pump power propagating in the PPLN waveguide. The anti-Stokes Raman scattering of 1560-nm pump is a broadband noise covering signal wavelength of 1540 nm. Thus, the Raman scattering noise within phase-matching bandwidth of PPLN waveguide is also up-converted to 775 nm. Even though the anti-Stokes Raman scattering is weaker than the Stokes Raman scattering and requires thermal phonons (i.e., can be suppressed by cooling the crystal), it may still contribute unwanted noise power and spoil mode-selective QFC. In the effort to reduce broadband Raman noise as much as possible, we used 0.035-nm-wide VBG-based 775-nm BPF from Optigrate.

4.4.4 Time-correlated single-photon counting (TCSPC) setup

To properly measure up-converted photon numbers, we used time-correlated single-photon counter (TCSPC) from PicoQuant (Picoharp 300E), as shown in Figure 4-20. The Si-based avalanche photodiode, also known as single-photon detector (SPD), generates an electrical pulse if a photon is detected. The TCSPC measures time delay between a trigger pulse (channel 1) and a pulse from SPD (channel 2) and generates histogram of measured photon arrival times. Note that the TCSPC registers at most one photon between the consecutive trigger pulses, ignoring second pulse within the trigger interval (~50 ns). Because the intervals between photons are not regular, but random (Poisson distribution), to ensure that only a single photon exists after a trigger pulse, the average photon number N has to be << 1 photon/pulse: in that case the single-photon counting probability is given by the average photon number N, whereas two-photon probability is ~ $N^2/2$ << N. In our measurement, the photon number to TCSPC is ~ 0.05 photon/pulse. The reference signal beam (1540nm) for triggering is obtained from a horizontally-polarized beam from the PBS in the signal path and is converted into electric signal by 1.2-GHz photodetector. Note that 1.2-GHz photodetector is sufficient for the generation of trigger pulse (our signal pulse is 400-ps long), because the TCSPC only responds to the downward slope of the pulse.

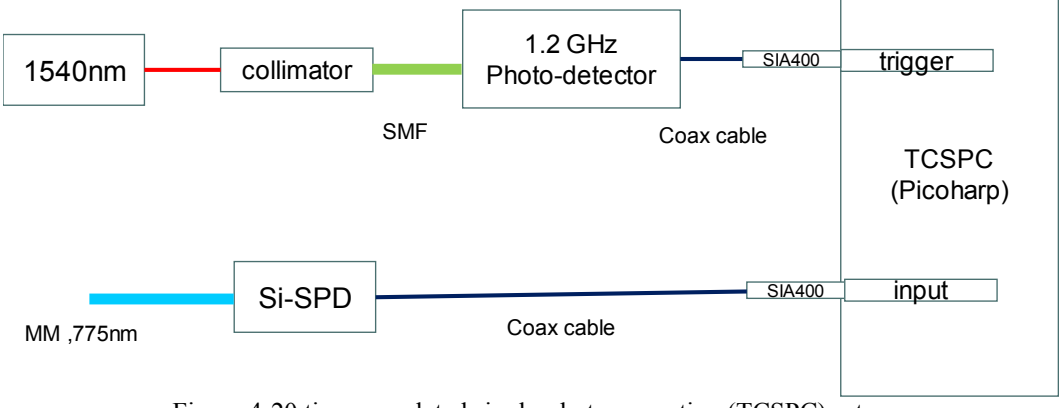

Figure 4-20 time-correlated single-photon counting (TCSPC) setup

4.4.5 Results / Discussion

To quantify the quality of single-photon demultiplexing, we measure the conversion efficiency and crosstalk. We define the internal conversion efficiency η_{int} as the SFG power divided by twice the signal power at the output of the PPLN waveguide (note that this definition is different from our previous definition of the internal conversion efficiency for classical beams, because our setup does not permit direct observation of depletion of the single-photon-level signal). For our case, signal power at the output of PPLN waveguide is –96 dBm, which is, in terms of signal photon number, 2×10^6 photons/sec. Thus, η_{int} is defined, in terms of photon number, as the ratio of up-converted photon number to the signal photon number at the PPLN output (in the absence of the pump). The actual up-converted photon number is found from the integration of measured histogram and correcting for the SFG-beam loss (e.g., quantum efficiency from SPD, losses from filters, and coupling loss to MMF). We measured histograms for 20 seconds with 4-ps time bin resolution and only pulse area (~3-ns-wide) is considered for integration to maximally suppress dark counts. The measured histogram is shown in Figure 4-21. We define the external conversion efficiency η_{ext} as the SFG power divided by twice the signal power at the input of the waveguide, to include the waveguide coupling and propagation losses. The crosstalk is computed as the ratio of the internal conversion efficiencies of the undesired and desired signal modes for a given pump mode. The results, listed in Table 4-3, indicate > 78% internal and > 34% external conversion efficiencies for the desired signal modes, and crosstalk better than –12 dB in all cases.

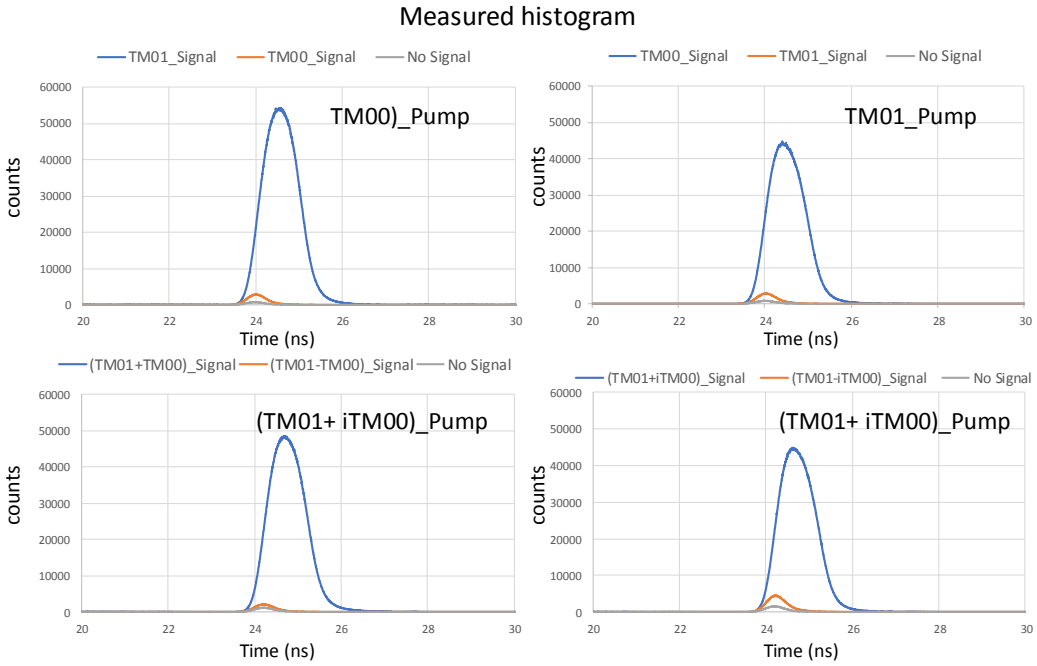

Figure 4-21 Measured histograms

Table 4-4 Internal and external photon conversion efficiencies and crosstalk

	signal	pump	η_{int}	η_{ext}	crosstalk
Desired	TM_{00}	TM_{00}	2.4%	1.1%	–15.4 dB
Undesired	TM_{01}	TM_{00}	84.3%	37.1%	
Desired	TM_{00}	TM_{01}	81.2%	35.7%	–14.4 dB
Undesired	TM_{01}	TM_{01}	2.9%	1.3%	
Undesired	$TM_{01} + TM_{00}$	$TM_{01} - TM_{00}$	2%	0.9%	–16 dB
Desired	$TM_{01} - TM_{00}$	$TM_{01} - TM_{00}$	78.7%	34.6%	
Desired	$TM_{01} + iTM_{00}$	$TM_{01} + iTM_{00}$	79.04%	34.8%	–12.4 dB
Undesired	$TM_{01} - iTM_{00}$	$TM_{01} + iTM_{00}$	4.5%	2.0%	

4.4.6 Conclusions

To summarize, we have experimentally demonstrated frequency up-conversion of selected spatial modes and mode superpositions of two-mode single-photon-level signals with > 78% internal conversion efficiency, better than −12 dB crosstalk, and > 10^2 ratio of signal to background photon noise in all cases. In the future, with several QPM gratings, mode-selective up-conversion can be extended to a larger mode space.

Chapter 5

CONCLUSIONS

In this dissertation, we extensively investigated selective frequency up-conversion of spatial modes for classical and quantum communication. It is enabled by sum-frequency generation (SFG), also known as quantum frequency conversion (QFC), because its fundamental unitary-transformation nature preserves quantum properties of the input signal after up-conversion, which can benefit a variety of quantum applications. The QFC allows the use of the Si-based single photon detector (SPD) having high quantum efficiency and low dark counts and also provide easier interface from fiber communication in telecom band to quantum memory in visible / near IR region. In classical applications, the spatially-selective QFC can be used as a reconfigurable de-multiplexer of spatial modes. Growing demand for higher information capacities of fiber optic links has lead to the emergence of new mode-division multiplexing (MDM) systems, which could greatly benefit from such a de-multiplexer.

Before attempting any experiments, we developed a theory for frequency conversion of selected signals based on SFG in a 1D waveguide (2D free space), followed by extensive numerical optimization. The results indicated that the selective up-conversion in 2D free space is feasible with limited performance. After that, our modeling has found that a 2D waveguide approach with proper quasi-phase matching (QPM) and waveguide dimensions is far more promising for selective up-conversion of spatial modes.

Such a waveguide in periodically-poled lithium niobate (PPLN) was custom-fabricated for us by Prof. Martin Fejer's group at Stanford. To evaluate our approach in both classical and quantum applications, several experimental demonstrations were performed on single signal modes and on superpositions of signal modes. We used a two-mode PPLN waveguide with 11-μm QPM grating period for all experiments. For the classical experiment with two signal modes generated by SLM, we observed more than 70% of internal conversion efficiency and better than –16-dB mode

crosstalk. The mode selection is done by choosing the pump spatial profile, which can be reconfigured by an SLM at up to a ~50 Hz rate without introducing any losses into the signal path. With several QPM gratings, mode-selective up-conversion can be extended to a larger mode space and used for dynamically reconfigurable mode demultiplexing of classical and quantum signals.

To see whether spatially-selective QFC is suitable for quantum application, we repeated the above experiment with single-photon-level signal (~0.1 photon/pulse) by attenuating signal by multiple neutral density (ND) filter. The several parasitic effects such as Raman scattering from PPLN waveguide, second harmonic generation (SHG) from strong pump, and amplified spontaneous emission (ASE) noise from EDFA can potentially prevent single-photon-level up-conversion. These undesired effects are suppressed by custom-made filters in the pump, signal, and SFG arms. As a result, we observed more than 70% internal conversion efficiency, better than –14 dB crosstalk, and $>10^2$ ratio of the signal to the background (Raman, SHG, and ASE) noise.

To verify the usefulness of the spatial-mode-selective frequency up-conversion in classical fiber optic communication, two experimental demonstrations were done: an experiment with signal modes transmitted through a few-mode-fiber (FMF) and an experiment with 10.7 Gb/s NRZ-modulated signal modes.

The experiment with a FMF is performed to see the compatibility of signal modes from a FMF with the modes of the PPLN waveguide. By combining fundamental-mode signal beam with a beam modulated by a phase plate we launch any superposition modes into the FMF. Using several telescopic lenses and a 1:2 one-dimensional beam expander to match the mode sizes between the PPLN waveguide and FMF, we observed more than 45% internal conversion efficiency and better than –14 dB crosstalk. The low internal conversion efficiency is mostly due to the mode size mismatch and can be improved by using better quality optics.

Finally, an experimental demonstration was done with 10.7 Gb/s non-return-zero (NRZ) modulated signal mode to see whether the mode-selective up-conversion is suitable for mode de-

multiplexing in the MDM communication system. Both TM_{00} and TM_{01} signal modes are modulated with 10.7 Gb/s NRZ data and decorrelated by introducing 1 km of single-mode fiber (SMF) into one mode's path. We measured both eye-diagrams and bit-error rates and observed that the de-multiplexing of a signal mode (e.g., TM_{00}) in the presence of both signal modes (e.g., TM_{00} and TM_{01}) showed ~2.5 dB power penalty at 10^{-9} bit-error rate, compared to the up-conversion of a single signal mode (e.g., TM_{00} without TM_{01}). This result indicate that our scheme is suitable for high-speed fiber links.

For the future work, two more experiments with the same PPLN waveguides are proposed. In the first experiment, 775-nm pump can generate spatially-entangled signal and idler photons at 1540 nm and 1560 nm. In the second experiment, a two-mode 10 Gb/s signal at 1540 nm is frequency-converted in the PPLN waveguide by 775-nm pump into 1560 nm idler, which can be used as an MDM wavelength converter / phase conjugator for future MDM communication links.

Chapter 6 References

1. P. Kumar, "Quantum frequency conversion," Optics letters **15**, 1476-1478 (1990).
2. J. Huang and P. Kumar, "Observation of quantum frequency conversion," Physical review letters **68**, 2153 (1992).
3. A. Eckstein, B. Brecht, and C. Silberhorn, "A quantum pulse gate based on spectrally engineered sum frequency generation," Optics express **19**, 13770-13778 (2011).
4. M. G. Raymer and K. Srinivasan, "Manipulating the color and shape of single photons," Physics Today **65**, 32-37 (2012).
5. Y.-P. Huang and P. Kumar, "Mode-resolved photon counting via cascaded quantum frequency conversion," Optics letters **38**, 468-470 (2013).
6. P. J. Mosley, A. Christ, A. Eckstein, and C. Silberhorn, "Direct measurement of the spatial-spectral structure of waveguided parametric down-conversion," Physical review letters **103**, 233901 (2009).
7. M. Karpiński, C. Radzewicz, and K. Banaszek, "Experimental characterization of three-wave mixing in a multimode nonlinear KTiOPO 4 waveguide," Applied Physics Letters **94**, 181105 (2009).
8. S. Armstrong, J.-F. Morizur, J. Janousek, B. Hage, N. Treps, P. K. Lam, and H.-A. Bachor, "Programmable multimode quantum networks," arXiv preprint arXiv:1201.6024 (2012).
9. M. Vasilyev and P. Kumar, "Frequency up-conversion of quantum images," Optics express **20**, 6644-6656 (2012).
10. P. S. Kuo, J. S. Pelc, O. Slattery, Y.-S. Kim, M. Fejer, and X. Tang, "Reducing noise in single-photon-level frequency conversion," Optics letters **38**, 1310-1312 (2013).
11. M. A. Albota and F. N. Wong, "Efficient single-photon counting at 1.55 μm by means of frequency upconversion," Optics letters **29**, 1449-1451 (2004).

12. R. T. Thew, H. Zbinden, and N. Gisin, "Tunable upconversion photon detector," Applied Physics Letters **93**, 071104 (2008).

13. M. Vasilyev, Y. B. Kwon, and Y.-P. Huang, "Highly mode-selective quantum frequency conversion in a slab waveguide," in *SPIE OPTO*, (International Society for Optics and Photonics, 2014), 89970O-89970O-89978.

14. M. Vasilyev, Y. B. Kwon, and Y.-P. Huang, "Spatial-Mode-Selective Quantum Frequency Conversion in a χ (2) Slab Waveguide," in *High Intensity Lasers and High Field Phenomena*, (Optical Society of America, 2014), JW2A. 52.

15. Y. B. Kwon and M. Vasilyev, "Mode-selective frequency up-conversion in a χ (2) waveguide," in *SPIE LASE*, (International Society for Optics and Photonics, 2014), 89640N-89640N-89648.

16. S.-K. Choi, M. Vasilyev, and P. Kumar, "Noiseless optical amplification of images," Physical review letters **83**, 1938 (1999).

17. E. Lantz and F. Devaux, "Parametric amplification of images: from time gating to noiseless amplification," IEEE Journal of Selected Topics in Quantum Electronics **14**, 635-647 (2008).

18. M. Annamalai and M. Vasilyev, "Phase-sensitive multimode parametric amplification in a parabolic-index waveguide," IEEE Photonics Technology Letters **24**, 1949-1952 (2012).

19. M. Vasilyev, M. Annamalai, N. Stelmakh, and P. Kumar, "Quantum properties of a spatially-broadband traveling-wave phase-sensitive optical parametric amplifier," Journal of Modern Optics **57**, 1908-1915 (2010).

20. M. Annamalai, N. Stelmakh, M. Vasilyev, and P. Kumar, "Spatial modes of phase-sensitive parametric image amplifiers with circular and elliptical Gaussian pumps," Optics express **19**, 26710-26724 (2011).

21. M. Annamalai, N. Stelmakh, P. Kumar, and M. Vasilyev, "Compact representation of the spatial modes of a phase-sensitive image amplifier," Optics express **21**, 28134-28153 (2013).

22. J. Midwinter, "Image conversion from 1.6 μ to the visible in lithium niobate," Applied Physics Letters **12**, 68-70 (1968).

23. M. Roelofs, A. Suna, W. Bindloss, and J. Bierlein, "Characterization of optical waveguides in KTiOPO4 by second harmonic spectroscopy," Journal of applied physics **76**, 4999-5006 (1994).

24. V. Delaubert, M. Lassen, D. Pulford, H.-A. Bachor, and C. Harb, "Spatial mode discrimination using second harmonic generation," Optics express **15**, 5815-5826 (2007).

25. J. R. Kurz, J. Huang, X. Xie, T. Saida, and M. M. Fejer, "Mode multiplexing in optical frequency mixers," Optics letters **29**, 551-553 (2004).

26. J. Kurz, X. Xie, and M. Fejer, "Odd waveguide mode quasi-phase matching with angled and staggered gratings," Optics letters **27**, 1445-1447 (2002).

27. J. D. Bierlein and H. Vanherzeele, "Potassium titanyl phosphate: properties and new applications," JOSA B **6**, 622-633 (1989).

28. T. Y. Fan, C. Huang, B. Hu, R. C. Eckardt, Y. Fan, R. L. Byer, and R. Feigelson, "Second harmonic generation and accurate index of refraction measurements in flux-grown KTiOPO 4," Applied optics **26**, 2390-2394 (1987).

29. R. Boyd, "Nonlinear Optics 3rd edn (New York: Academic)," (2008).

30. P. J. Winzer, "Making spatial multiplexing a reality," Nature Photonics **8**, 345-348 (2014).

31. Y. B. Kwon and M. Vasilyev, "Spatial-mode-selective quantum frequency conversion in nonlinear waveguides," in *SPIE Optics+ Optoelectronics*, (International Society for Optics and Photonics, 2015), 95050O-95050O-95057.

32. C. Langrock, E. Diamanti, R. V. Roussev, Y. Yamamoto, M. M. Fejer, and H. Takesue, "Highly efficient single-photon detection at communication wavelengths by use of upconversion in reverse-proton-exchanged periodically poled LiNbO 3 waveguides," Optics letters **30**, 1725-1727 (2005).

33. P. Manurkar, N. Jain, M. Silver, Y.-P. Huang, C. Langrock, M. M. Fejer, P. Kumar, and G. S. Kanter, "Multidimensional mode-separable frequency conversion for high-speed quantum communication," Optica **3**, 1300-1307 (2016).

34. Y. B. Kwon, M. Giribabu, L. Li, S. C. Samudrala, C. Langrock, M. Fejer, and M. Vasilyev, "Experimental demonstration of spatial-mode-selective frequency up-conversion in a multimode χ (2) waveguide," in *Lasers and Electro-Optics (CLEO), 2016 Conference on*, (IEEE, 2016), 1-2.

Chapter 7 Biographical Information

Young received his Bachelor in Electrical Engineering from Hong-Ik University (Seoul), his Master of Science degree in Electrical Engineering from University of Texas at Arlington (2010). In 2011, he joined a group of Prof. Michael Vasilyev for his doctoral research which is funded by DARPA Quiness program. He served as a president of Optical Society of America (OSA) student chapter for 2016-2017. His research interest is frequency up-conversion, nonlinear waveguides, and fiber-optic communication.